

Benchtop μ XRF as a tool for speleothem trace elemental analysis: Validation, limitations and application on an Eemian to early Weichselian (125–97ka) stalagmite from Belgium

Vansteenberghe, Stef; De Winter, Niels; Sinnesael, Matthias; Xueqin, Zhao ; Verheyden, Sophie; Claeys, Philippe

Published in:
Palaeogeography, Palaeoclimatology, Palaeoecology

DOI:
[10.1016/j.palaeo.2019.109460](https://doi.org/10.1016/j.palaeo.2019.109460)
[10.1016/j.palaeo.2019.109460](https://doi.org/10.1016/j.palaeo.2019.109460)

Publication date:
2020

License:
CC BY-NC-ND

Document Version:
Proof

[Link to publication](#)

Citation for published version (APA):
Vansteenberghe, S., De Winter, N., Sinnesael, M., Xueqin, Z., Verheyden, S., & Claeys, P. (2020). Benchtop μ XRF as a tool for speleothem trace elemental analysis: Validation, limitations and application on an Eemian to early Weichselian (125–97ka) stalagmite from Belgium. *Palaeogeography, Palaeoclimatology, Palaeoecology*, 538, 1-18. [109460]. <https://doi.org/10.1016/j.palaeo.2019.109460>, <https://doi.org/10.1016/j.palaeo.2019.109460>

Copyright

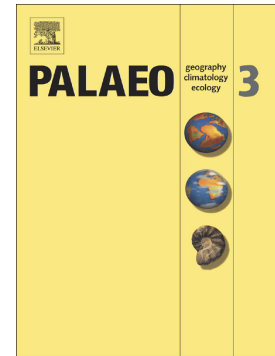
No part of this publication may be reproduced or transmitted in any form, without the prior written permission of the author(s) or other rights holders to whom publication rights have been transferred, unless permitted by a license attached to the publication (a Creative Commons license or other), or unless exceptions to copyright law apply.

Take down policy

If you believe that this document infringes your copyright or other rights, please contact openaccess@vub.be, with details of the nature of the infringement. We will investigate the claim and if justified, we will take the appropriate steps.

Benchtop μ XRF as a tool for speleothem trace elemental analysis: Validation, limitations and application on an Eemian to early Weichselian (125–97 ka) stalagmite from Belgium

Stef Vansteenberge, Niels J. de Winter, Matthias Sinnesael, Zhao Xueqin, Sophie Verheyden, Philippe Claeys



PII: S0031-0182(17)31165-3

DOI: <https://doi.org/10.1016/j.palaeo.2019.109460>

Reference: PALAEO 109460

To appear in: *Palaeogeography, Palaeoclimatology, Palaeoecology*

Received date: 15 November 2017

Revised date: 23 October 2019

Accepted date: 12 November 2019

Please cite this article as: S. Vansteenberge, N.J. de Winter, M. Sinnesael, et al., Benchtop μ XRF as a tool for speleothem trace elemental analysis: Validation, limitations and application on an Eemian to early Weichselian (125–97 ka) stalagmite from Belgium, *Palaeogeography, Palaeoclimatology, Palaeoecology* (2019), <https://doi.org/10.1016/j.palaeo.2019.109460>

This is a PDF file of an article that has undergone enhancements after acceptance, such as the addition of a cover page and metadata, and formatting for readability, but it is not yet the definitive version of record. This version will undergo additional copyediting, typesetting and review before it is published in its final form, but we are providing this version to give early visibility of the article. Please note that, during the production process, errors may be discovered which could affect the content, and all legal disclaimers that apply to the journal pertain.

Benchtop μ XRF as a tool for speleothem trace elemental analysis: validation, limitations and application on an Eemian to early Weichselian (125-97 ka) stalagmite from Belgium.

Stef Vansteenberge^{*1}, Niels J. de Winter¹, Matthias Sinnesael¹, Zhao Xueqin² Sophie Verheyden¹ and Philippe Claeys¹

¹Department of Analytical Chemistry, Vrije Universiteit Brussel, Pleinlaan 2, 1050 Brussels (Belgium)

²Institute of Environment and Resources, Southwest University of Science and Technology, 621010 Mianyang, (China)

*corresponding author: stef.vansteenberge@vub.be

KEYWORDS

X-ray fluorescence, speleothem, trace elements, paleoclimate, last interglacial

ABSTRACT

Variations of trace element (e.g. Mg, Sr, Ba, Fe, Zn etc.) concentrations along a speleothem's growth axis constitute important paleoclimate proxies. The use of laboratory micro X-ray fluorescence spectrometry as a fast and cheap alternative for conventional mass spectrometry techniques for trace element analysis on speleothems has been explored in the past and yielded satisfactory results. However, within the speleothem community there is need for an in-depth investigation of the full potential of this analytical technique. Compared to other types of paleoclimate archives, benchtop (μ)XRF analysis on speleothems is analytically more challenging because of the high-crystalline speleothem matrix and the low abundance of the elements of interest. In this study, several speleothem samples with differences in mineralogy (calcite versus aragonite) and composition are investigated. Various instrumental parameters are tested and recommendations are made for future studies applying (μ)XRF analysis to speleothems. Quantification based on a multiple standard calibration and an assessment of the error is carried out. Through validation with mass spectrometry techniques, it is confirmed that benchtop μ XRF devices are able to generate speleothem trace element records. Successful results were obtained for Sr, Mg and Fe, while Zn and Ba were quantified in samples characterized by high concentrations. Nevertheless, caution has to be taken when interpreting the results, due to the presence of diffraction caused by the crystallinity of the samples. The elements which provide reliable results are sample specific and depend on the type of matrix and elemental abundance. These findings are applied on an Eemian to early Weichselian stalagmite from the Han-sur-Lesse Cave, Belgium. Time series were constructed for Mg and Sr, creating a multiproxy dataset together with previously obtained stable isotope ($\delta^{13}\text{C}$ and $\delta^{18}\text{O}$) ratios,

growth-rate and stalagmite morphology. It appears that Mg and Sr are not primarily controlled by prior calcite precipitation, but rather by changes in vegetation activity above the cave.

INTRODUCTION

Speleothems constitute one of the most important continental paleoclimate archives and their use has been proven successful in numerous paleoclimate reconstructions (e.g. Bar-Matthews et al., 1999; Wang et al., 2001; Genty et al., 2003; Verheyden et al., 2008a; Boch et al., 2011, Van Rangelbergh et al., 2015; Vansteenberghe et al., 2019). Besides the well-established $\delta^{13}\text{C}$ and $\delta^{18}\text{O}$ stable isotope ratio proxies (McDermott, 2004; Lachniet 2009; Wong and Brecker, 2015), variations in trace element concentrations along the speleothem growth axis also yield crucial information about diverse climate-controlled processes (Fairchild et al., 2000; Verheyden et al., 2000; Fairchild et al., 2006; Fairchild and Treble, 2009; Wynn et al., 2014). For instance, variations in bedrock-derived (alkaline earth) elements such as magnesium (Mg), strontium (Sr) and barium (Ba) have been attributed to changes in prior calcite precipitation (PCP). PCP is defined as the precipitation of calcite upstream of the site of speleothem deposition. These changes are directed by drip water availability and therefore primarily reflect changes in the amount of local meteoric precipitation (Fairchild et al., 2000). This effect is even observed on a seasonal scale (Johnson et al., 2006; Jamieson et al., 2016; Vansteenberghe et al., 2019). Concentrations of other trace elements, for instance phosphorous (P), zinc (Zn), yttrium (Y) and lead (Pb), are mainly soil—derived (Borsato et al., 2007), and are therefore indicators of environmental changes (Fairchild and Treble, 2009; Frisia et al., 2012, Jamieson et al., 2016, Vansteenberghe et al., 2019). These soil-derived elements bind to natural organic matter in the soil and serve as a proxy for vegetation activity above the cave and the amount of seasonal soil-flushing (Hartland et al., 2012; Wynn et al., 2014). Combined stable isotope and trace element records have gained more attention in speleothem studies that aim to reconstruct past hydroclimate. In order to satisfy this new demand for high resolution chemical analyses, novel techniques, such as micro X-ray fluorescence (μXRF) analysis, are employed to acquire the large amount of trace element data needed to produce robust time series.

Over the last decades, XRF analysis has been shown to be an excellent technique for fast and non-destructive analysis of elemental abundance in various types of geological materials, including sediment cores (Richter et al., 2006; Weltje and Tjallingii, 2008) and bivalve shells (Kurunczi et al., 2001; de Winter and Claeys, 2016; de Winter et al., 2017a). The pioneering work of Frisia et al. (2005), Borsato et al. (2007), Wynn et al. (2014) and Vanghi et al. (2019) illustrates the major potential of synchrotron radiation μXRF (SR- μXRF) for trace element analysis on speleothems, even down to the micrometer-resolution. In comparison, although SR- μXRF enables higher resolution (sub-

micrometer scale) measurements, the available number of synchrotron radiation facilities is limited and therefore not always accessible within the time frame of a research project. Laboratory μ XRF devices therefore provide a valuable, accessible alternative for the study of trace element compositions of speleothems at the micron to millimeter scale and may help to prepare for further SR measurements.

A wide range of XRF instruments exists, ranging from XRF core scanners, benchtop models and portable XRF scanners that can even be used in the field. The advantages of μ XRF analysis are that it requires little to no sample preparation and is non-destructive, fast and relatively inexpensive. For example, a single, quantitative data point used in this study takes about 90 s to collect, with sample preparation limited to the polishing of the flat sample profile. Semi-quantitative compositional information can be gathered even more rapidly by employing fast 2D XRF mapping. Despite these advantages, it has to be pointed out that the geochemical purity of speleothem CaCO_3 and the highly crystalline matrix makes the application of laboratory μ XRF challenging and may induce analytical biases.

Several types of crystal fabrics (e.g. columnal, fibrous and microcrystalline) have been identified in speleothem samples (Frisia et al., 2000 and references therein). The presence of these fabrics has been shown to depend on drip rate, carbonate saturation state and drip water chemistry and may contain information about past climate variability (Frisia et al., 2000; 2002; Matthey et al., 2010; Frisia, 2015). Even different minerals (e.g. calcite and aragonite) may be present in a single speleothem, sometimes related to replacement of aragonite by calcite after deposition (Frisia et al., 2002). Since direct (i.e. without destructive sampling) spectroscopic methods such as XRF produce spectra that contain information related to both chemical composition and matrix crystallinity, samples with the same chemical composition but different crystal fabrics will yield different results, unless this interference of crystallinity can be resolved (e.g. Sutton et al., 1986). In addition, the effects of processes such as adsorption, inclusion and incorporation of trace elements in the speleothem may vary due to different degrees of porosity due to changes in crystal fabrics, causing the chemical composition to vary as a function of the crystal fabric.

One of the earliest tests of laboratory μ XRF analysis on speleothems is provided by Dandurand et al. (2011), in which various types of cave deposits were measured. Work by Finné et al. (2015) also showed the ability of μ XRF to identify flood layers in speleothems based on the detection of Iron (Fe) and Silicon (Si). Both these studies used an XRF core scanner. The study from Buckles and Rowe (2016) was the first to actually determine optimal measurement conditions for speleothems in terms of instrumental parameters with a semi-portable XRF scanner. They also created calibration curves to

transform the semi-quantitative XRF data into quantitative results. Furthermore, a detailed discussion of the effect of measurement conditions on lab-based μ XRF results on carbonates was provided by de Winter et al. (2017b), paving the way for quantitative analysis. The possibility of obtaining quantitative results encourages the use of μ XRF as an inexpensive, fast and non-destructive alternative for analytical techniques such as digestion inductively coupled plasma mass spectrometry (ICP-MS), laser ablation ICP-MS (LA-ICP-MS) and ICP optical emission spectrometry (ICP-OES). Recent studies, however, still lack a thorough methodological validation or specific guidelines, especially for elements other than Sr (e.g. Cui et al., 2012; Wu et al., 2012; Buckles and Rowe, 2016) .

In this study, multiple tests of XRF measurements using a lab-based μ XRF setup were conducted under different measurement conditions and on a wide range of samples, including stalagmites and stalagmites of different ages and with mixed mineralogy. The results of these tests are evaluated by comparison with trace element data measured using ICP-MS techniques on the same samples. In this way, recommendations are provided for future μ XRF-based speleothem trace element analyses, including suggestions and/or guidelines on how to 1) determine optimal measurement parameters, 2) identify which elements can be measured in a reliable way, 3) to recognize the effects of sample conditions (e.g. porosity and crystallinity). Finally, guidelines are proposed for quantifying μ XRF results from speleothems and to assess the uncertainty of these results. These findings are then applied to a case study carried out on a stalagmite of Eemian to early Weichselian age from Han-sur-Lesse Cave, Belgium, of which stable isotope ratios were already reported in and discussed by Vansteenberge et al. (2016).

ANALYTICAL BACKGROUND

The X-ray fluorescence analysis technique uses an X-ray source to excite the sample material and measures the returning X-ray radiation spectrum to characterize the sample composition. Absorption of X-ray radiation by atoms in the sample material causes their electrons to be excited. After excitation, the electrons return to their lower energy state by emitting X-rays, a process known as fluorescence. The energy of the fluorescent X-ray depends on the electron configuration of the atom and therefore bears a signature characteristic for the element. In XRF analysis, fluorescent X-rays emitted by an excited sample are used to determine the elemental composition of the sample, and the amount of fluorescence photons counted in the peaks, i.e. the intensity, is proportional to the concentration of the element in question. The relationship between intensity and elemental concentration is described by the Sherman equation (Sherman, 1955), which was manipulated into the Fundamental Algorithm for application on XRF analysis by Rousseau (Rousseau, 1984a; 1984b; Rousseau and Bouchard, 1986; Rousseau and Boivin, 1998). For a more in-depth discussion of the

physical principles of XRF analysis, we refer to the work of Jenkins (1999), Beckhoff et al. (2006), Shackley (2011) and Gauglitz and Moore (2014).

Theoretically, XRF analysis provides the user with quantitative results, because the intensity of the fluorescent X-rays are proportional to the abundance of an element in the sample. After detection of the XRF spectra, element peaks in the spectra are deconvoluted and absolute concentrations can be calculated. By using the standard-less Fundamental Parameter (FP; based on the Fundamental Algorithm) quantification method, based solely on the theoretical fluorescence behavior of selected elements (Potts and Webb, 1992), one should be able to deduce sample concentrations directly from the theoretical principles. This makes XRF analysis the only analytical technique that allows such close integration of theoretical base into the experimental results (Rousseau and Boivin, 1998). However, for composite samples, the complexity of considering material-specific matrix effects, X-ray absorption and X-ray enhancement warrants the use of empirical approximations in order to simplify the calculations used for quantification. It is recommended to apply matrix-specific calibrations with well-known reference materials, especially when aiming towards accurate quantitative results. A comprehensive study of the effect of measurement conditions and strategies on the results of μ XRF analysis on carbonates was carried out by de Winter et al. (2017b). The authors demonstrated that an optimal compromise can be found between increasing measurement time of individual XRF spectra (which increases signal-to-noise ratios) and increasing the number of measurements (which improves the achievable spatial sampling density). This optimum is determined by trying various measurement conditions such as different X-ray beam excitation energies and the integration times on a matrix-matched standard with known chemical composition. This allows the user to find the optimal measurement condition after which both the reproducibility and accuracy cannot be improved significantly by changing the measurement parameters (Time of Stable Reproducibility, or TSR, and Time of Stable Accuracy, or TSA). In the present study, we build further on these findings and propose analytical guidelines to obtain reliable quantified micro-XRF results on speleothems.

METHODS

Speleothem samples

For this study, a wide range of different speleothems were selected from the archive of former samples measured at the Vrije Universiteit Brussel (Belgium). Additional samples were provided by Geotop, Québec (Canada) and Southwest University of Science and Technology, Mianyang (China). The samples differ in trace element composition, mineralogy (calcite vs. aragonite), age (Holocene, last glacial, last interglacial), location (Belgium, Mexico, China) and growth rate (up to 1 mm yr^{-1}). All samples are presented in Fig. 1, with locations of the μ XRF measurements presented in this paper

indicated in red. An overview of the specifics of each sample is provided in Table 1. Mex-1 is the lower part of stalagmite retrieved from Cacahualmilpa Cave, Mexico. The speleothem is approximately 50 ka in age. Han-8 is a 180 mm long stalagmite of last interglacial age retrieved from Han-sur-Lesse Cave, Belgium. Trace element concentrations of Han-8 have already been determined with LA-ICP-MS (S. Verheyden, unpublished data) and can therefore be used to validate the μ XRF method. CS-2 is a stalactite from Mao'er Cave, China. This sample is of particular interest because of its mixed calcite-aragonite mineralogy. P16 is part of a core retrieved from the Proserpine stalagmite (Han-sur-Lesse Cave, Belgium). The complete core has been studied in detail by Verheyden et al. (2006) and Van Rampelbergh et al. (2015). P16 was included in this study to investigate the ability of μ XRF to study annually laminated speleothems at high resolution (25 μ m). Han-9 is a 678 mm long, candle-shaped stalagmite from Han-sur-Lesse cave, Belgium. A detailed description of the sample is provided by Vansteenberghe et al. (2016). In this work, Han-9 is used as subject of a case study to demonstrate the ability of benchtop μ XRF devices to create speleothem trace element time series. All speleothem samples were polished manually using progressively fine silicon-carbide polishing discs and finished with a fine (< 5 μ m) Al_2O_3 powder polishing with deionized water (following Van Rampelbergh et al., 2015). MicroXRF measurements were carried out directly on the polished slabs.

In addition, uncovered thin sections of samples Han-9, CS-2 and P16 were created for microscopic analysis by TS Lab and Geoservices (Cascina, Italy). Samples Han-9, CS-2 and P16 were chosen for their variable mineral textures and the presence of both calcite and aragonite (in CS-2). Thin sections were studied by plain polarized (PPL) and cross-polarized (XPL) transmitted light microscopy using a Meiji MT9930L trinocular polarizing microscope equipped with a digital camera (Meiji Techno co. Ltd., Saitama, Japan). The crystal fabrics in each thin section were fully mapped by capturing overlapping microscope images under 25x magnification, and stitching these images together using the Photomerge tool in Adobe Photoshop CC 2015 (Adobe Systems Inc., San Jose, CA, USA). In addition, higher magnification (40x, 100x and 400x) micrographs were created to study crystal fabrics in detail. Based on these micrographs, crystal fabrics in these samples were identified using coding in the calcite fabric classification scheme proposed by Frisia (2015).

μ XRF instrumental setup

All XRF analyses were carried out on a M4 Tornado (Bruker, Germany) benchtop μ XRF device. A scheme of the M4 set-up is shown in de Winter and Claeys (2017). The M4 Tornado is a μ XRF spectrometer with a motorized X-Y-Z sample stage which, in contrast to setups previously used on speleothems (Dandurand et al., 2011; Cui et al., 2012; Wu et al., 2012; Finné et al., 2015; Buckles and Rowe, 2016), is able to operate under moderate vacuum conditions (20 mbar). The main advantage

of measuring under vacuum conditions is that fluorescence X-rays, especially low-energy X-rays, will be less severely attenuated by air between the X-ray source and the detectors and the sample on their way to and from the sample (Shackley, 2011). This is important for the detection of elements of which the main fluorescence peak is situated in the lower energy range of the spectrum. This is generally the case for elements with atomic numbers below 16, such as Mg, Al, Si, S and P, which are often of interest in speleothem studies (Fairchild and Treble, 2009). The source of the M4 Tornado consists of a 30 W Rh anode metal-ceramic X-ray tube with maximum voltage of 50 kV. Unless stated otherwise, all measurements in this study are carried out with a source voltage of 50 kV and source current of 600 μ A. Focusing of X-rays is done by a poly-capillary lens resulting in a final spot size of 25 μ m (calibrated for molybdenum-K α radiation). Since the M4 Tornado is an energy dispersive, single-focus setup, the actual dimensions of the X-ray spot parallel to the sample surface as well as the depth of material contributing to each spectrum (related to the attenuation length) varies with varying X-Ray photon energy (see Beckhoff, 2006). Two silicon drift detectors with an energy resolution ≤ 145 eV (FWHM, Full Width at Half Maximum, for manganese-K α) are used to count the returning X-rays. These detectors are placed such that the angle between the incident X-Ray beam hitting the sample from the X-Ray source and the outgoing X-Ray beam hitting the detector is 90°. This alignment allows for optimal capture of fluorescent X-ray photons and limits background radiation (see de Winter and Claeys, 2016). The M4 set-up is equipped with three different aluminum (Al) source filters: 12, 100 and 630 μ m thick, one aluminum-titanium filter of 100 and 25 μ m thick and one aluminum-titanium-copper filter with thicknesses of 100, 50 and 25 μ m. The Bruker M4 Tornado operates with the Bruker Esprit XRF software package, which allows quantification of XRF spectra. Little preparation is needed for the speleothem samples, as μ XRF only requires polished sample surfaces of samples with a large enough thickness to assume infinite sample thickness. This assumption holds if the thickness of the sample equals or exceeds three times the attenuation length of the element fluorescing at the highest energy (in this study Sr, with an attenuation length of ~ 250 μ m), in which case only 5% of the X-ray radiation penetrates the full thickness of the sample, 5% of which (0.25% of the initial intensity) subsequently makes it back to the detector (Rousseau et al., 1984b; 1998). Even so, caution has to be taken to obtain a smooth and level speleothem surface for the XRF measurement, as irregularities on the sample surface (e.g. high-porosity speleothems) cause uncontrolled scattering of X-rays away from the detector, resulting in random changes in count rates and increases in the amount of background counts (Buckles and Rowe, 2016). The M4 Tornado setup allows for different types of measurements, such as single point measurements, line scans and area maps (e.g. de Winter and Claeys, 2017; de Winter et al., 2017b).

Quantification of μ XRF spectra

The areas described by peaks in the XRF energy spectrum (which plots X-ray counts per second against the energy of the X-rays; see Figure 4) are proportional to the abundance of elements in the sample. To estimate the concentration of each element from the measured spectrum, the Esprit software makes use of a peak deconvolution algorithm to integrate the net intensity of the peak and the Fundamental Parameter (FP) algorithm to determine absolute elemental concentrations based on the Fundamental Algorithm (Sherman, 1955; Rousseau, 1984a; 2013). In this study, a matrix-matched calibration is carried out using a set of 7 carbonate reference materials spanning a wide range of trace element concentrations: CCH-1 (Université de Liège, Belgium), COQ-1 (US Geological Survey, Denver, CO, USA), CRM393 (Bureau of Analyzed Samples Ltd, Middlesbrough, UK; BAS), CRM512 (BAS), CRM513 (BAS), ECRM782 (BAS) and SRM-1d (National Institute of Standards and Technology, Gaithersburg, MD, USA). Calibration curves are constructed based on averages and standard deviations of 20 μ XRF point measurements of 90 s integration time, which is sufficient for the Time of Stable Reproducibility (TSR) to be reached (de Winter et al. 2017b; see also Background chapter above). An overview of all measured and certified values of the standards is provided as supplementary data. To incorporate both measurement errors and errors on the certified values into the calibration curves, a linear Deming regression is applied (Adcock, 1878; Kummell, 1879; Deming, 1943). Regression curves are calculated using the “deming” package in the open-source computational software package R (R Core Team, 2013). Statistics and results of the regressions are summarized in Fig. 2, Table 2 and the R-script used to create the regressions is provided as supplementary data. Pearson’s r values of calibration curves of Mg, Sr, Ba, Mn and Fe used for data analysis in this study always exceeded 0.98.

Validation of quantified μ XRF results

To test the performance of the μ XRF method presented in this study, i.e. to check accuracy of the quantified μ XRF results, two trace elements transects on the same speleothem were measured using both μ XRF and LA-ICP-MS:

A first comparison is carried out for sample Han-8 (Fig. 1, Table 1), on which a 25 mm long transect is measured with both methods. The LA-ICP-MS measurements were previously carried out at the Royal Africa Museum (Tervuren, Belgium). Measurements were done on a Fisons-VG frequency quadrupled Nd-213 YAG laser ($\lambda = 266$ nm) coupled to a Fisons-VG 214 PlasmaQuad II+ mass spectrometer. Data were calibrated using both the NIST 610 (Pearce et al., 1997) and the USGS MACS1. Calibration (including blank subtraction and drift correction) was performed offline by using Ca as internal reference. Laser ablation was carried out by using a spot size of 50 μ m. Details of LA-ICP-MS operating conditions can be found in Lazareth et al. (2003). A total of 599 data points were collected on this Han-8 speleothem, yielding a spatial resolution of ~ 0.04 mm. Uncertainties were

calculated using the relative standard deviation of NIST 610. Afterwards, a similar transect was analyzed with the M4 Tornado μ XRF set-up at the Vrije Universiteit Brussel (Belgium). The μ XRF transect comprises a total of 258 single point analysis (0.1 mm resolution), measured for 90 s each.

A second comparison was carried out on sample P16. The ~14 mm long LA-ICP-MS profile, collected at Ghent University (Belgium), and consists out of 287 data points (0.05 mm resolution). This data was already available from an earlier study (Vansteenberge et al., 2019) and a full description of the LA-ICP-MS analytical procedure can be found herein. The same transect was measured with μ XRF at the maximum spatial resolution of 25 μ m, resulting in 587 data points.

RESULTS AND DISCUSSION

Crystal fabrics

Detailed microscopic observation of samples Han-8, CS-2 and P16 (Fig. 3) shows that there is significant heterogeneity in crystal fabric both within and between samples. The CS-2 sample contains aragonite (Fig. 3E-F), which is present as a needle-like acicular texture, and is found only in the basal part of the speleothem. In some places, the aragonite texture is replaced by calcite, resulting in lenses of mosaic calcite fabric (Fig. 3D-F). The remainder of CS-2 and the major part of Han-8 consist of columnar calcite with an open structure (characterized by a higher degree of porosity and inclusions; see Frisia, 2015; Fig. 3A-F). The edges of both CS-2 and Han-8 are marked by a layer of micritic or microsparitic calcite fabric. Sample Han-8 also consists primarily of open structure columnar calcite with an outer edge of mosaic calcite. A layer of compact columnar calcite separates these two structures (Fig. 3A-B). Finally, P16 consists fully out of compact columnar calcite with large crystals with welded crystal boundaries without observable porosity. Interestingly, several marked shifts in crystal orientation occur within this texture, which can be freely observed under cross polarized light (Fig. 3G-I).

Speleothem μ XRF spectrum characteristics

Background signal and elemental peaks

The μ XRF energy spectra of 2 point measurements (90 s) conducted on speleothem sample MEX-1 (Table 1, Fig. 1) are displayed in Fig. 4. The general shape of the XRF spectra is determined by the X-ray source and sample characteristics (i.e. elemental abundance and the sample matrix). The broad plateau, occurring between 5 and 30 keV is known as Bremstrahlung, which is caused by the occurrence of backscatter without exciting the sample, and is a major feature in the background spectrum (Shackley, 2011). Additionally, Rayleigh peaks are generated through the elastic scattering of X-rays coming directly from the X-ray tube source and radiated from the sample without any

change in energy (Potts and Webb, 1992). The energy of these peaks depends on the X-ray source. In the case of a Rh tube, the Rayleigh peaks are always located at 20.216 (K_{α}) and 22.724 keV (K_{β}) (Fig. 4). Compton peaks are caused by the inelastic scattering of X-rays from the source. The inelastic scattering results in some energy loss compared to elastic scattering, causing these peaks to be located at slightly lower energies compared to the Rayleigh peaks (to the left of the Rayleigh peaks, Fig. 4). Also, the width of the Compton peaks is slightly higher compared to Rayleigh peaks as a result of this energy loss which causes more variation in energy (Potts and Webb, 1992). Fluorescence peaks of elements always occur at their characteristic energy levels. For example, the main fluorescence peak of Sr (K_{α}) is located at 14.165 keV and a smaller, secondary peak (K_{β}) has an energy of 15.836 keV (Fig. 4).

Sum and Escape peaks

Given the high amount of calcium (Ca) in most speleothems (up to 40 wt%), the main peak (K_{α} at 3.692 keV) and the secondary peak (K_{β} at 4.013 keV) of Ca always dominate the spectrum for CaCO_3 speleothems. This will cause additional artificial peaks to occur: the sum peaks and the escape peaks (Fig. 4). The escape peak is generated when Si atoms in the detector absorb energy coming from the X-rays emitted by elements with a high abundance, in this case Ca. The escape peaks for Ca are located at 1.952 keV and 2.273 keV, which can be calculated by subtracting the energy of $K_{\alpha}(\text{Si})$ (=1.740 keV) from that of $K_{\alpha}(\text{Ca})$ and $K_{\beta}(\text{Ca})$ (see above). Theoretically, all elements have escape peaks, especially those of lighter elements, but escape peaks tend to be more prominent for elements with higher abundance in the spectrum, such as Ca in speleothem samples. The Ca escape peak zone partly overlaps with the element peak (K_{α}) of P, located 2.014 keV (Fig. 4). This overlap results in problems during the deconvolution of P and causes concentrations of this element to be more difficult to quantify in samples with high Ca and comparatively low P concentrations. The second set of artificial peaks are sum peaks, caused by two photons arriving at the detector at the exact same time. The energy at which the sum peaks are located can be calculated by adding up the energies of the specific photons. For Ca, this means that sum peaks will be located at 7.384 keV ($K_{\alpha} + K_{\alpha}$) and 7.705 keV ($K_{\alpha} + K_{\beta}$), which causes an overlap with Ni ($K_{\alpha} = 7.480$). The sum peak of $K_{\beta} + K_{\beta}$ at 8.026 keV can often be neglected as K_{β} photons are much less common than K_{α} photons. Sum peaks can also occur if 2 photons of different elements hit the detector at the same time, but given the dominant abundance of Ca compared to other elements these can be neglected in speleothem samples. Some XRF software packages, such as the Esprit software of the M4 Tornado, automatically correct for the presence of sum and escape peaks by subtracting them from the spectrum through an estimation of their intensity based on the net amount of Ca counts (Fig. 4). However, in some cases these artificial Ca peaks need to be processed manually (e.g. Finné et al., 2015).

Diffraction peaks

One issue of benchtop XRF analysis on speleothems that has not received much attention before is the high amount of X-ray diffraction caused by the crystallinity of the calcite (or aragonite) matrix. This diffraction of X-rays results in peaks in the XRF spectrum that do not correspond to elements, known as diffraction or Bragg peaks. Diffraction peaks are characteristic for a given crystal orientation, which means that they can be located at different energy levels in the spectrum, depending on the orientation of the speleothem sample and the crystals within the sample. Diffraction peaks can be problematic for the correct identification of certain elements, as they can overlap with elemental peaks (Fig 3). The microscopy results shown in **Fig. 3** show why the nature of these Bragg peaks can cause problems, as crystal orientation (and therefore the location of diffraction peaks on the spectrum) varies demonstrably within and between speleothem samples. Two main characteristics of diffraction peaks can be used to identify them from element peaks. First of all, diffraction peaks strongly depend on the analyzed medium, so their location within the energy spectrum changes when different parts of the sample are measured. This is shown in Fig. 4, where the diffraction peaks of Point 2 occur at a different energy compared to Point 1. Additionally, diffraction peaks can be discriminated from element peaks because they tend to be broader than element peaks (Fig. 4). The energy, and therefore the location on the spectrum, of diffraction peaks is a function of crystal orientation relative to the X-Ray beam, meaning that rotation of the sample should cause XRD peaks on the spectrum to change, while XRF peaks remain unchanged (Sutton et al., 1986). The non-destructive character of XRF measurements allows this rotation of the sample after which the same sample volume can be analyzed.

The problem with diffraction peaks is that they can overlap with and be mistaken for element peaks, leading towards a failure of the peak deconvolution algorithm. Once a diffraction peak overlaps with an element peak, it compromises the integration of that element peak and therefore affects the XRF quantification. Diffraction peaks are very common between 6 and 13 keV (Fig. 4), where peaks of Ba, titanium (Ti), manganese (Mn), Fe, copper (Cu), nickel (Ni) and Zn occur. Therefore, these elements should always be treated carefully when analyzing speleothems. Dandurand et al. (2011) deduced from μ XRF maps that the distribution of elements like Cu and Zn followed the crystalline fabric. However, this assumption is not supported by this study. Instead, it is suggested that an overlap of diffraction and element peaks of Zn and Cu occurred. Diffraction is mostly determined by the fabric and the crystallographic orientation of the calcite crystals within the speleothem, which would cause the distribution of these elements to resemble the crystallographic orientation. Although the spectrum was not provided by Dandurand et al. (2011), similar maps to those presented by Dandurand et al. (2011) can easily be reproduced for Cu and Zn. Fig. 6 clearly shows the difference

between Sr, of which the distribution reflects the speleothem layering, and Cu and Zn, which represent diffraction. This same pattern can be observed when integrating the Rayleigh peak over the same map, whose intensity is affected by crystal orientation (Beckhoff, 2006; compare Fig. 6E with 4F). This issue demonstrates that proper identification of the different peaks within a spectrum is crucial for a correct interpretation of XRF results, especially when working with highly crystalline materials such as speleothems. Fig. 6 also illustrates that elemental maps are a quick way to identify the elements that are likely to be overlapped by diffraction peaks within the spectrum. Such interpretation is simplified by combining XRF measurements with microscopic observations, such as is shown in Fig. 3.

Thin section-based microscopy enables the identification of different mineral textures and associated crystal orientations in the speleothem sample, which can be matched with patterns in XRF data (such as the maps in Fig. 6). This approach can be used to demonstrate whether the observed variability in XRF spectra is related to changes in the speleothem fabric or whether it reflects independent changes in elemental concentrations. Comparison with microscopic observations shows that limitations of the spot size of benchtop XRF used in this study (25 μm) prevent this technique to resolve the finest scale variability in mineral fabrics (e.g. individual crystals and inclusions on the nano-scale). The sample volume analyzed during any XRF measurement made using this technique is therefore likely to include a mix of multiple crystals. Furthermore, some crystal fabrics (e.g. dendritic or microcrystalline fabrics) are known to contain high amounts of crystal defects and inclusions, which cannot be resolved by benchtop XRF alone and may influence the XRF spectrum as well as the actual chemical composition of the crystal (Frisia et al., 2000). Therefore, contrary to SR-XRF, analyses carried out using current benchtop XRF systems on complex aggregate crystalline samples such as speleothems should always be combined with microscopic observations and identifications of crystal fabrics.

Calcite versus aragonite mineralogy

The eventual shape of an XRF spectrum largely depends on the matrix of the investigated material and the elemental composition of the sample. Therefore, theoretically, a distinction between calcite and aragonite should be possible based on the shape of the μXRF spectrum. To confirm the presence of both calcite and aragonite in sample CS-2, X-ray diffraction analysis was carried out at the Katholieke Universiteit Leuven (Belgium). The XRD spectra are shown in Supplementary Figure 1. The whiter and more porous parts of the stalactite are made up of aragonite whereas the dense white and brownish parts consist of calcite (Fig. 1). The distinction between acicular aragonite and mosaic-textured calcite fabrics is also observed in Fig. 3. XRF analysis on CS-2 was carried out in two ways.

First, an area measurement was undertaken. This results in a map with each pixel representing a single XRF measurement. The disadvantage of such area maps is that each point is only measured for a restricted amount of time (in this case 50 ms), which, especially in the case of speleothems, is insufficient to obtain quantitative data for certain elements. Therefore, a second analysis consisting of a transect of single point measurements was carried out. The results are shown in Figure 5. A first observation is that the spectrum of an aragonite measurement (Fig. 7) clearly shows less diffraction peaks compared to regular calcite spectra (Fig. 4 and Fig. 5). From the transects measured on the polished surface of CS-2 it is evident that the aragonite mineralogy in the speleothem has higher concentrations of Sr and Ba. Fe is concentrated within the fine brownish layers, which represent more porous microcrystalline mosaic calcite laminae within the stalactite containing higher amounts of detrital material in their porosity (e.g. in the form of colloidal particles). The same qualitative observation can be made by comparing the XRF map of Sr with the color scan of the speleothem, which shows that the areas where aragonite is the predominant phase (light color) coincide with higher Sr concentrations (orange/red in the map). However, care must be taken during such interpretations, as nano-scale inclusions, including nano-aragonite, can be present within other carbonates (Wenk et al., 1983; Frisia, 1994; Frisia et al., 2002). While SR-XRF theoretically allows the combination of X-Ray Diffraction and XRF analyses to be carried out on the same sample volume (Frisia et al., 2012), potentially solving this issue, this is not possible using benchtop XRF or ICP-MS techniques. This demonstrates that, unless the measurement technique enables this type of sub-micron scale control on both chemical and mineralogical variability in the samples, a detailed assessment of the mineralogy of the sample, e.g. through thin section investigations and/or XRD analysis, is required to enable careful interpretation of the chemical results.

Measurement time

It has been previously shown that measurement time is an important parameter affecting the XRF spectra (Buckles and Rowe, 2016; de Winter et al., 2017b). Increasing measurement time generally increases the signal-to-noise ratio. However, at a certain point, there will be no significant improvement, as recognized by de Winter et al. (2017b). To illustrate this for speleothems, a point on sample Han-9 was consecutively analyzed for 0.3, 0.5, 1, 2, 5, 10, 20, 30, 60, 90, 120, 240 and 600 s. Fig. 8 shows the evolution of the net counts for each element of the speleothem spectrum with time, plotted as a percentage of the total counts. The ideal measurement time should be long enough for the asymptotic value to be reached while being kept as low as possible for practical considerations. For Al, Si, P, Sulphur (S), Zn and Sr, the percentage does not change significantly after 60 s. However, Mg and Fe still increase, even up to 600 s. To account for this, and to increase the sensitivity for Mg in particular, a minimum measurement time of 90 s is deemed sufficient for the purpose of this

paper. This minimum measurement time also influences the measurement strategy. As mentioned before, the M4 Tornado setup can perform point analysis, continuous line scanning and area maps. When measuring line scans and area maps, the XYZ stage is continuously moving, which limits the measurement time at any one location to maximum ~ 1 s (movement speed > 0.025 mm/s). As shown in Fig. 8, this is insufficient for most elements of interest. Therefore, in this study, the measurement strategy consists of single point analysis for a dwelling time of at least 90 s per point.

Filters

In XRF analysis, source filters are often used to reduce the background signal, eliminate diffractive artifacts and remove tube characteristic lines (Elam et al., 2010). Source filters are commonly made up of metals such as Al, Cu and Ti and vary in thickness. To investigate the impact of different filters on speleothem samples, one single spot on sample Han-9 is measured consecutively with each available filter for 90 s. Fig. S3 shows that Al filters with progressively increasing thicknesses tend to decrease the count rate of the reflected X-rays in the middle-energy range, and thus also decrease the influence of diffraction on the spectrum. The use of Al filters with thicknesses ≥ 100 μm results in a reduction of count rates for elements in the low-energy spectrum, i.e. $< K_{\alpha}(\text{Ca})$ for example Mg, to a level that prevents successful peak deconvolution. Buckles and Rowe (2016) stated that speleothem carbonate samples require the use of Al-Ti-Cu, which serves to block a large proportion of the Ca emissions. Indeed, the count rate of Ca is significantly decreased by using an Al-Ti-Cu 100-50-25 filter but this filter also prevents the detection of any other trace element with peak energies below 10 keV (e.g. Mg, Al, S, Fe, Zn; Fig. S3), which is a significant drawback. An experimental μXRF study on bivalve calcite carried out by de Winter and Claeys (2017) has shown that the use of Al-Ti-Cu filters increases the signal-to-noise-ratio in the 5 to 15 keV region, but significantly decreases the count rate. Therefore, we chose not to use filters in the present study.

Quantification and calibration

A schematic overview of the quantification and calibration process presented in this paragraph is provided in Figure 10. All measurements on the M4 Tornado μXRF are initially quantified by the Bruker Esprit software package. Within this software quantification process, a single-standard calibration of initial concentration values that are obtained from applying the FP equation on the intensities of the deconvoluted XRF peaks is added. This single-standard calibration is applied to correct for matrix effects that cause the initial FP quantification to be offset from actual sample concentrations. The calibration is made by repeatedly measuring a matrix-matched reference material. In the case of calcium carbonate measurements, the CRM393 limestone certified reference material is used. These measurements are then quantified using the FP quantification and the result

is compared to the known concentrations of the reference material. Wherever quantified values are offset from the reference values, correction factors are applied to correct the result. This is done iteratively for all elements of interest until the result of the corrected quantification method matches the reference concentrations. The correction factors determined for each element are applied on all measurements of the same matrix. Results of previous methodology tests indicate that a single-standard calibration is not always sufficient to correct for the matrix effect of μ XRF analysis (de Winter et al., 2017b). This is especially true for elements whose peaks interfere with other element peaks. Therefore, a multi-standard calibration needs to be carried out after the initial quantification with the XRF software.

The results of Deming regression for the construction of calibration lines for a range of trace elements measured using μ XRF using carbonate reference materials are provided in Table 2. These calibration curves, determined on multiple standards, are used to calibrate the data after the software quantification (Fig. 10). Calibration curves for a selection of elements are given in the supplementary material (Fig. S2). High Pearson's r (r) values for all but a few elements (Al, Si, S, K and Cr) shows that linear calibration lines fit the data very well. This indicates that the offset of uncalibrated results, caused by matrix effects in carbonates, can be approximated by a linear correction. Furthermore, slope constants in Table 2 show that the size of the correction needed is different between elements, with some elements (e.g. Mg, Fe and Sr) having slopes close to 1, while other elements (e.g. P and Ba) have slopes deviating more from the 1:1 line. In the case of P, this can be explained by the overlap of the $K\alpha$ peak of P with the escape peak of Ca (Fig. 4), causing parts of the peak of P to be interpreted as escape peak and the P peak to be underestimated by the peak deconvolution algorithm. Similar problems might force the slope of the Ba calibration line, as several XRF peaks of Ba overlap with other elements such as Ti and Vanadium (V). These complications occur in all XRF measurements on carbonates and have been incorporated into the calibration. This, together with the fact that XRF measurements on reference materials are carried out by multiple point measurements on a homogeneous sample surface should render the calibration curves presented in this paper applicable on a wide range of carbonate samples.

Assessment of the uncertainty

As demonstrated above, results of XRF analysis are inherently prone to over-interpretation if not treated with care. It is therefore of utmost importance to define the uncertainty of the method. Some steps have been taken towards a universal definition of uncertainty in XRF analyses, and new criteria for determining the conditions of reliable measurement have been proposed such as time of stable reproducibility (TSR) and time of stable accuracy (TSA; de Winter et al., 2017b). Because of the

large influence of surface and matrix effects on the XRF spectrum, it is also essential that reproducibility tests aiming to provide a realistic measure for measurement uncertainty should be carried out on various different spots of a homogeneous, matrix-matched standard (i.e. in the same way measurements on reference materials are carried out in this study). This is the only way to incorporate differences in surface properties, machine performance and sample matrix as well as uncertainties in the calculations of the software into the measurement error (Buckles and Rowe, 2016; de Winter and Claeys, 2016; de Winter et al., 2017b). The reproducibility standard deviation calculated from the variation between these measurements reflects the total uncertainty of a spot measurement on the sample. The obtained relative standard deviations (RSD) represent the error of the measurement (Fig. 10). Care must be taken to ensure that all measurement conditions (e.g. source energy, integration time and chamber vacuum) of these reproducibility measurements are equal to the conditions used to measure the sample. Furthermore, since the concentration of elements in the sample influences the reliability with which it can be measured using μ XRF, concentrations of the standard used for reproducibility testing should approach the concentrations of the sample that is investigated (de Winter et al., 2017b). In the case of speleothem samples, the BAS-CRM393 standard is used for this purpose. It is preferred over, for example, the COQ1 of USGS, which has much higher Sr concentrations (12 000 ppm) than is naturally present in speleothems (10-1000 ppm; see Table 1 for average values in samples in this study). The RSD's of each element measured with the μ XRF setup, representing the error of the μ XRF measurements, are provided in the supplementary material (Table S2). The uncertainty of the speleothem μ XRF analysis is represented by an error bar in the concentration plots (e.g. Fig. 10-12). It is important to note that reproducibility errors calculated this way are significantly higher than so-called machine errors commonly provided by XRF software, which only take into account uncertainties associated with the peak deconvolution and quantification steps (see de Winter and Claeys, 2017). In addition to errors on individual XRF measurements, we also provide estimates of the Lower Limit of Detection (LLD) based on the error on the calibration for each element and deconvolution errors on certified carbonate reference materials in Table 2. These LLD's show that the presented μ XRF technique just barely allows the measurement of Mg concentrations (under vacuum conditions, and if concentrations are high enough to surpass the detection limit, compare Table 1 and 2), while other elements of interest such as Mn, Fe, Zn and Sr have LLD's well below typical concentrations found in speleothems.

Validation

Figure 11 shows a comparison of a 25 mm transect on sample Han-8 that was measured with both LA-ICP-MS and μ XRF. The quantification and calibration of the μ XRF data was done following the

procedure described above. LA-ICP-MS data was available for Mg, Al, P, Zn, Sr, Ba, Pb and U. μ XRF data are available for Mg, Al, Zn, Sr and Ba. Concentrations of Pb and U are too low to be detected by this μ XRF setup (average of 235 and 86 ppb, respectively) and overlap with the element peak of P and the Ca escape peak. For Mg and Sr, the absolute concentrations obtained by LA-ICP-MS and μ XRF appear to be in good agreement. Sr concentrations have been measured before in a reproducible way using a different μ XRF setup (Buckles and Rowe, 2016). Sr yields good results because the Sr concentration in speleothems tends to be rather high (50 – 1000 ppm) while the detection limit is low (1-10 ppm). Also, the Sr peak is not overlapped by diffraction, at least not in the spectra used in this study (Fig. 4). Mg, on the other hand, has proven to be a lot more difficult because the main Mg peak ($K_{\alpha} = 1.254$ keV) is located in the lower energy range of the spectrum. Lighter energy X-rays are more easily scattered and more rarely reach the sample and the detector. Furthermore, the Rh source used by the M4 Tornado XRF setup produces lower quantities of X-rays with low (<3 keV, “soft” X-rays) and high (>20 keV) energies, causing elements that fluoresce outside the 3 - 20 keV range to be more difficult to detect and quantify (see Fig. S3). This means that there is less radiation to excite Mg in the sample and that less fluorescent X-rays of Mg reach the detector. However, the ability to operate under vacuum conditions (20 mbar), sufficiently long measurement time and relatively high Mg concentrations in the sample significantly increases the potential of detecting and measuring Mg and other light elements, which require the detection of these “soft” X-rays (low-energy radiation). This is evidenced by the comparison between μ XRF and LA-ICP-MS data shown in Fig. 11, which are in good agreement for most of the record although μ XRF analysis seems to overestimate Mg concentrations in some part of the record (e.g. 0 – 5 mm). From Fig. 10, it can be deduced that μ XRF does not perform equally well for Ba, Zn and Al. The concentrations of these elements are consistently overestimated by the μ XRF technique compared to the LA-ICP-MS technique. In the case of Zn and Ba, this is due to an overlap of diffraction peaks with the element peaks, as shown in the spectra (Fig. 10). These diffraction peaks are mistaken for element peaks during peak deconvolution, reducing the accuracy of the measurement. However, good results for Ba were obtained for the aragonite sample CS-2 (Fig. 7). The main reason is the higher concentration of Ba in aragonite, which was already observed in other calcite-aragonite speleothems (Wassenburg et al., 2012). Although the results of CS-2 were not validated with other analytical techniques, the spectrum was checked manually and no overlap of the Ba element peak with diffraction peaks occur (Fig. 7). The lack of correlation for Al likely result from the low energy of the main Al peak ($K_{\alpha} = 1.487$) and the very low concentration of Al in the sample (average of ~11 ppm according to the LA-ICP-MS data, which is below the LLD of the μ XRF technique; see Table 2).

A second comparison was carried out on sample P16. This seasonally layered speleothem displays seasonal variations in Mg, Sr, Ba, Zn, Y, Pb and U as shown in earlier LA-ICP-MS measurements (Vansteenberge et al., 2019). μ XRF analyses at maximum resolution of 25 μ m showed that Y, Pb and U concentrations were too low to be quantified with our μ XRF setup, and that overlap with diffraction peaks occurs for Ba. The Mg, Zn and Sr results show that the μ XRF technique has the potential to reproduce the results obtained by LA-ICP-MS (Fig. 11). Especially the performance of μ XRF for Zn is remarkable in this sample. Although absolute concentrations determined with μ XRF are slightly higher, the method tracks the seasonal variations very well. The high amount of Zn in this speleothem sample compared to most speleothems (see Regattieri et al., 2016; Vansteenberge et al., 2019) and the absence of overlap with diffraction peaks enable a reliable measurement of Zn. As mentioned above, Zn is generally hard to measure because the element peak is located in a part of the energy peak where diffraction peaks are very common (Fig. 4; Fig. 6). Quantitative Zn profiles measured using benchtop μ XRF have, to the extent of our knowledge, not been reported so far in speleothems, in contrast to profiles in bivalve shells with a similar micro XRF setup (de Winter et al., 2017a).

For Mg, the scatter of the μ XRF data is larger compared to the LA-ICP-MS data but running averages appear to be in good agreement ($r = 0.71$; p -value $< 10^{-22}$), especially for the parts before between 0 and 8 mm (Fig. 11). After 8 mm, the correlation slightly deteriorates. A similar observation is made for Sr. An explanation for this may be that small surface imperfections such as porosity, common in speleothems, influences the quality of the data because they result in additional scattering of the X-rays (Beckhoff, 2006; de Winter and Claeys, 2017; Buckles and Rowe, 2016), which tends to play a larger role when working at higher resolutions. However, no noticeable change in crystal fabric or porosity is observed during thin section analysis (**Figure 3**). The fair agreement with the results of the more established LA-ICP-MS technique in this example as well as the reproduction of the seasonal changes in the record, illustrate the potential of μ XRF to produce high resolution (i.e. 25 μ m) trace element records. It must be noted that this spatial resolution cannot be reached for all elements measured using μ XRF as smoothing of the records (by means of a moving average) to reduce the scatter on some of these records (e.g. Mg) compromises the spatial resolution (see Fig 12).

Recommendations for future XRF measurements on speleothems

By testing the capabilities of a benchtop μ XRF device on various types of speleothem samples under different measurement conditions, as well as validating the acquired trace element data series, the following recommendations can be made for future (μ)XRF measurements on speleothems:

1) Combine μ XRF measurements with microscopic observations to detect changes in crystallography of the speleothem. This information helps to interpret the μ XRF spectra and detect interference of diffraction, especially when working with transient measurements (line scans or maps). Additional higher-resolution techniques, such as SR-XRF, EBDS and TEM could be included in speleothem studies to shed more light on the relationship between chemistry and microstructures in the samples, if available.

2) A good measurement starts with a good sample. Sample surfaces should be polished as smooth as possible, and the amount of irregularities (e.g. speleothem porosity) is preferentially low.

3) If possible, XRF analyses under vacuum conditions are preferred. This allows lighter elements such as Mg to be measured reliably.

4) Always check the XRF spectrum. This enables the identification of non-elemental peaks (e.g. sum peaks, escape peaks and diffraction peaks) that could potentially overlap element peaks, which lead to misinterpretation of the obtained data. It is advised in transient measurements to review each individual spectrum because changes in crystal orientation lead to changes in the location of the diffraction peaks in the spectrum. However, for large datasets (e.g. > 100 points) it becomes time consuming to check each spectrum, so some spectra can be selected at random or at suspicious points (e.g. suspiciously high counts of certain elements).

5) For reliable XRF measurements on speleothems, following instrumental conditions are proposed:

- Vacuum conditions
- Use maximum available source energy
- No source filters
- Multiple detectors (if available)
- Point-by-point analyses as opposed to transient line scans
- Minimum of 90 s measurement time (although more sophisticated setups may allow TSA and TSR to be reached with lower integration times)

6) Apply a standard-based quantification and calibration with matrix-matched standards. The multiple standard calibration presented in this study can also be used for calcium carbonate materials other than speleothems.

Case study: Han-9 trace element record

We used the M4 Tornado μ XRF to analyse the the Eemian-Weichselian Han-9 speleothem from the Han-sur-Lesse cave in Belgium (Vansteenberghe et al., 2016) for trace elements. Measurements are done on the first (125-117ka) and second (113-107ka) growth phases, and consisted of individual points along the 50 cm long central growth axis with a spatial resolution of 50 μ m. The last part of growth phase 2 is measured at a higher resolution (25 μ m between consecutive spots) to account for the diminished growth rate. Each point is analyzed for 90 s with a 50 kV 600 μ A Rh source. No filters are applied. Quantification of the individual point spectra is done using the aforementioned quantification method and values are calibrated using the presented calibration curves (Table 2 and supplementary material Fig. S2).

Spectrum

A spectrum acquired from Han-9 stalagmite is shown in Fig. S3. Clear element peaks are observed for Sr and Mg. Other elements, such as Fe, Zn and Ba overlap with diffraction peaks. Therefore, the XRF results of these elements are not reliable. Overlap of the Ca escape peak has affected the P peaks. Peaks for Al and S could be identified as well. No validation of the obtained XRF data with other analytical techniques was carried out for Han-9. Comparative XRF and LA-ICP-MS analyses on the Han-8 speleothem, which grew in the same cave and is similar in mineralogy and morphology (Fig. 10), have shown that the XRF technique yields accurate data for Sr and Mg, while analyses of Al, Zn and Ba are problematic (see **Validation**), and S data could not be confirmed. The μ XRF dataset in this case study is therefore limited to Mg and Sr.

Trace element time-series

The trace element time-series of Mg and Sr are shown in Fig. 12 together with $\delta^{13}\text{C}$ and $\delta^{18}\text{O}$ time-series as published in Vansteenberghe et al., (2016). In growth phase 1 (~126-121 ka), both Mg and Sr records display significant variations. The records show different centennial to millennial trends with very low correlations among the different proxy records. Comparison of the variations of the different records was carried out by calculating Pearson's correlation coefficients (r), for the entire records and for the two growth phases separately (Table 3). Only significant ($p < 0.05$) correlations are discussed. The highest degree of correlation is observed between Mg and $\delta^{13}\text{C}$, yet the r is only -0.19. In the second growth phase, Mg concentrations are lower and fairly constant, given that the amplitude of variations is close to the uncertainty. In contrast, Sr displays an important decrease towards ~110 ka followed by an increase between ~110 and ~107 ka. A clear negative correlation between $\delta^{13}\text{C}$ and Sr ($r = -0.64$) is observed, while both Mg and Sr show a weak positive correlation with $\delta^{18}\text{O}$ ($r = 0.32$ and $r = 0.40$, respectively), no significant correlation is observed between Mg and Sr trends.

Control on Sr and Mg variations

Variations in bedrock-derived trace elements such as Mg and Sr are often related to changes in hydrology of the epikarstic system, inducing prior calcite precipitation (PCP) processes. Since the partition coefficients of Mg and Sr in speleothem calcite are < 1 (Day and Henderson, 2013), these elements are enriched in the remaining fluid when PCP occurs, causing a subsequent enrichment in the speleothem. A higher degree of PCP is interpreted to reflect dryer periods (Fairchild et al. 2000; Fairchild and Treble, 2009). Kinetic processes and PCP, related to water availability were demonstrated as the main factor controlling Mg and Sr content of water and calcite in the Père Noël (PN) cave elsewhere in the Han-sur-Lesse karstic system (Verheyden et al., 2008b). The PN speleothem displayed similar time-series for $\delta^{18}\text{O}$, $\delta^{13}\text{C}$, Mg/Ca and Sr/Ca. However, in Han-9, a negative correlation only prevails between Sr and $\delta^{13}\text{C}$ in the second growth phase. Vegetation activity is identified as the primary control on $\delta^{13}\text{C}$ variations in Han-9 (see discussion in Vansteenberge et al., 2016; 2019), with more positive $\delta^{13}\text{C}$ values during dryer and/or colder periods when vegetation is less active. If PCP were to be the control on the Sr variations, a positive correlation would be expected, which is not the case here. This means that either the $\delta^{13}\text{C}$ change is related to a temperature decrease or PCP is not the primary controlling factor on the observed variations in Sr concentrations. The latter is in agreement with the lack of correlation between Mg and Sr. Obviously, both trace elements are controlled by different factors, demonstrating that PCP, affecting both elements, is not the main factor.

Instead, changes in vegetation activity (and consequently soil CO_2 fluxes influencing limestone dissolution), driven by changes in the precipitation regime above the cave, combined with processes involving differential dissolution of calcite and dolomite (incongruent dissolution) may explain variations in Sr and Mg. The absence of strong in-phase (e.g. because of PCP, Fairchild and Treble, 2003) or anti-phase (e.g. related to wet/dry conditions and incongruent dissolution; Huang et al., 2001; Vansteenberge et al., 2019) correlations between Mg and Sr complicates the interpretation of the Han-9 Mg record. However, the strong anticorrelation between Sr and $\delta^{13}\text{C}$ (Fig. 13), and the synchronous variations in speleothem morphology parameters observed, for example, in coincidence with the onset of the Late Eemian Aridity Pulse (LEAP) at the end of growth phases 1 strongly suggest that Sr variability is controlled by climate-related processes. Additionally, changes in calcite precipitation rate, infiltration rate of water through the epikarst and aerosol deposition have also been shown to influence Sr and Mg concentrations in speleothems (Belli et al. 2017).

CONCLUSIONS

This study investigated and confirmed the potential of laboratory μ XRF analysis for measuring trace element concentrations in speleothems. Although the μ XRF operational procedures are fast and straightforward, the vast amount of data that can be obtained this way is prone to misinterpretation if not combined with careful sample characterization. The main challenges of analyzing speleothems with μ XRF are the dominance of Ca compared to the trace elements and the occurrence of matrix specific effects (such as diffraction) that alter the spectrum. We have found that which elements can be measured in reliable way is very sample specific, warranting careful sample-by-sample assessment of the results. This can easily be done by verifying the individual spectra and by validating with other analytical techniques. In this study, different measurement conditions are tested and the most reliable results are obtained with a Bruker M4 Tornado μ XRF scanner by doing point-by-point transects with a (Rh) source energy of 50 kV and 600 μ A and a measurement time of 90 s for each point. The use of filters is not advised because they lower the intensity of the XRF spectrum and make it harder to detect key elements such as Ba, Fe and Zn. It is recommended to apply a matrix-matched standard-based calibration even after a single-standard matrix-matched quantification. In our sample set, reliable results are obtained (and validated with LA-ICP-MS) for Mg, Sr, Ba, Fe and Zn, however, it is not unlikely that, in the near future and with better instruments, quantification other elements (e.g. K, S, Cl, Mn) will become possible too. The presented case study has demonstrated the ability of μ XRF to rapidly construct high-resolution trace element profiles that can complement the traditional $\delta^{13}\text{C}$ and $\delta^{18}\text{O}$ stable isotope proxies. A multiproxy interpretation (stable isotopes, trace elements and speleothem morphology) of stalagmite Han-9 has shown that prior calcite precipitation is not responsible for the observed variations in Sr and Mg, since lower values occur during dryer periods. Instead, because of the strong anti-correlation with $\delta^{13}\text{C}$, it is hypothesized that the primary control on Sr and Mg in Han-9 is a decrease in soil efficiency. This leads to a decrease in CO_2 in the infiltrating water, resulting in lower host rock dissolution rates and providing less Mg and Sr to the drip water.

Data availability

All data used for this study are available in the open-access online repository Zenodo (<https://zenodo.org/record/3516695>).

Acknowledgements

The authors would like to thank two anonymous reviewers for their comments that helped improve the manuscript. We thank editor dr. Paul Hesse for moderating the review process. All authors thank the Domaine des Grottes de Han S.A. for allowing us to sample the speleothems and carry out other fieldwork. S. Vansteenberge thanks D. Pinti and the Geotop Institute for the Mexican speleothem sample. This research was funded by the VUB Strategic Research Program (S. Vansteenberge), IWT Flanders (N.J. de Winter), FWO Flanders (M. Sinnesael), National Natural Science Foundation of China (Z. Xueqin) and the Hercules Foundation Flanders (acquisition of the μ XRF instrumentation).

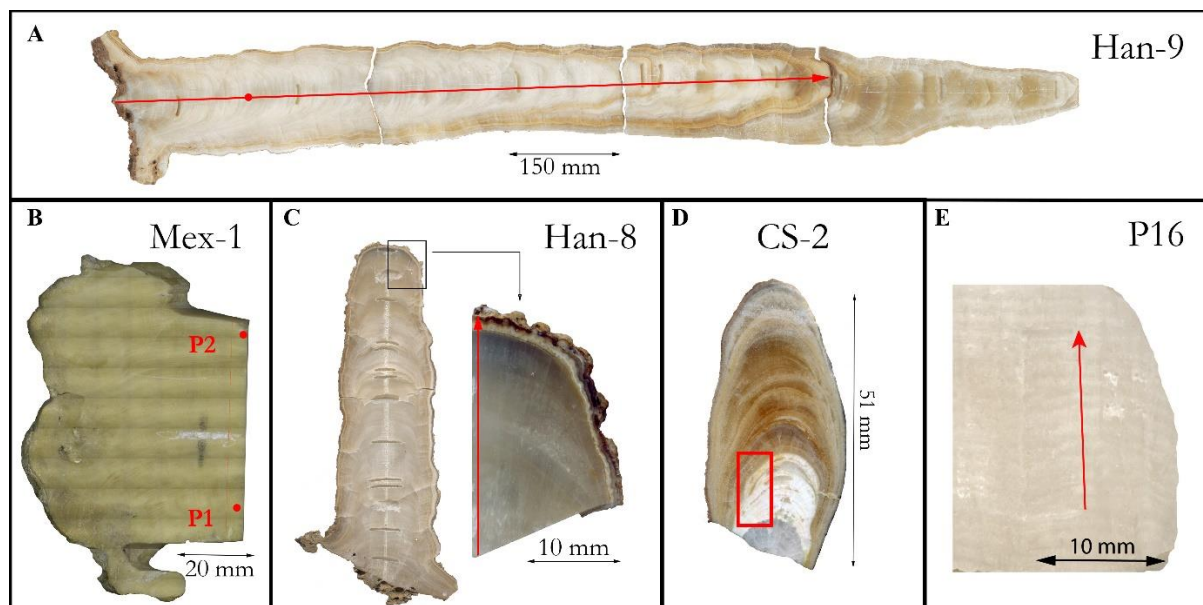


Figure 1: Speleothem samples used in this study: (A) Han-9 stalagmite, (B) Mex-1 stalagmite, (C) Han-8 stalagmite, (D) CS-2 stalactite and (E) P16, part of the Proserpine stalagmite. The scale varies for each sample and is displayed in the figure. Locations of the XRF measurements are shown in red. Additional information on each sample is provided in table 1.

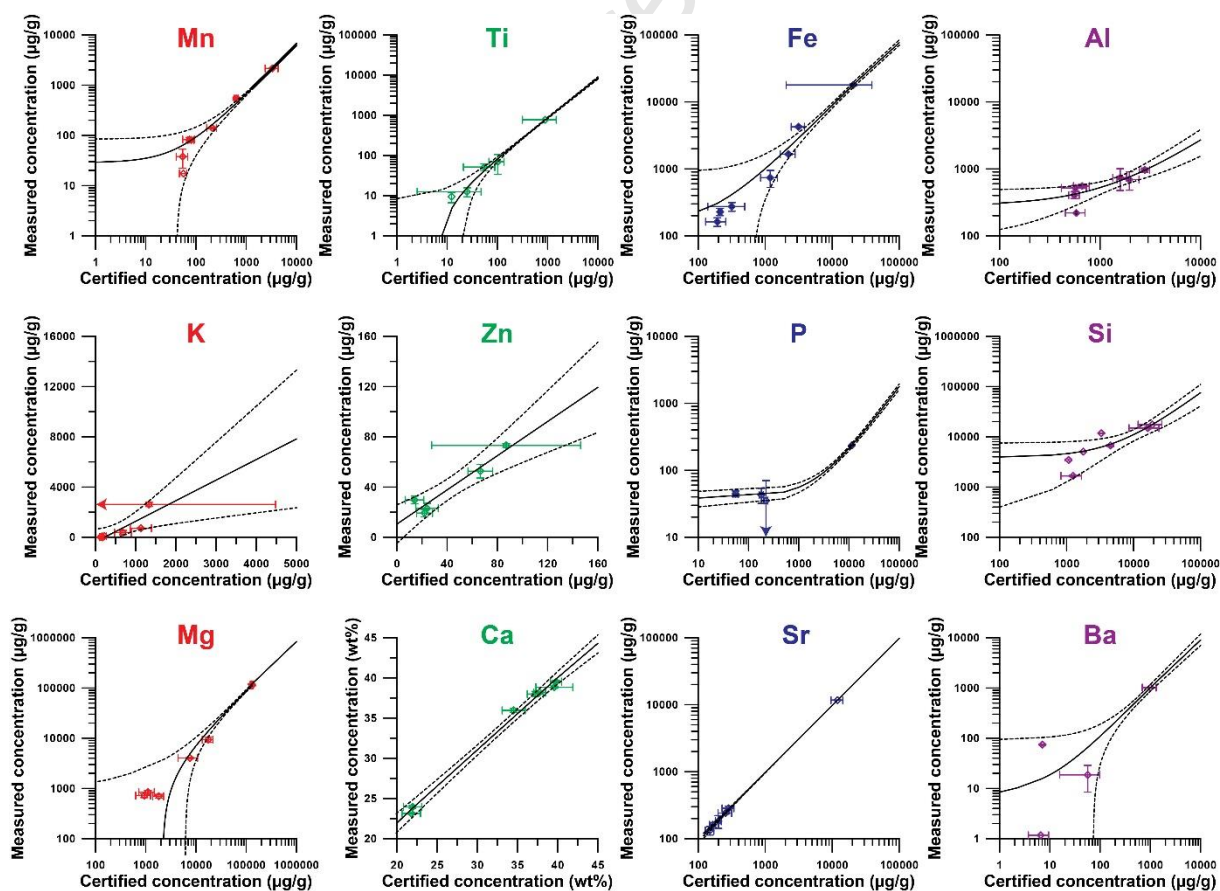


Figure 2: Overview of the results of measurements of matrix-matched certified reference materials used to calibrate XRF data in this study. Note that some axes (most notably of calibration plots of

detrital elements such as Mn, Ti, Fe and Al) are in log-scale, causing the linear regression curves fitted through these data to appear curved.

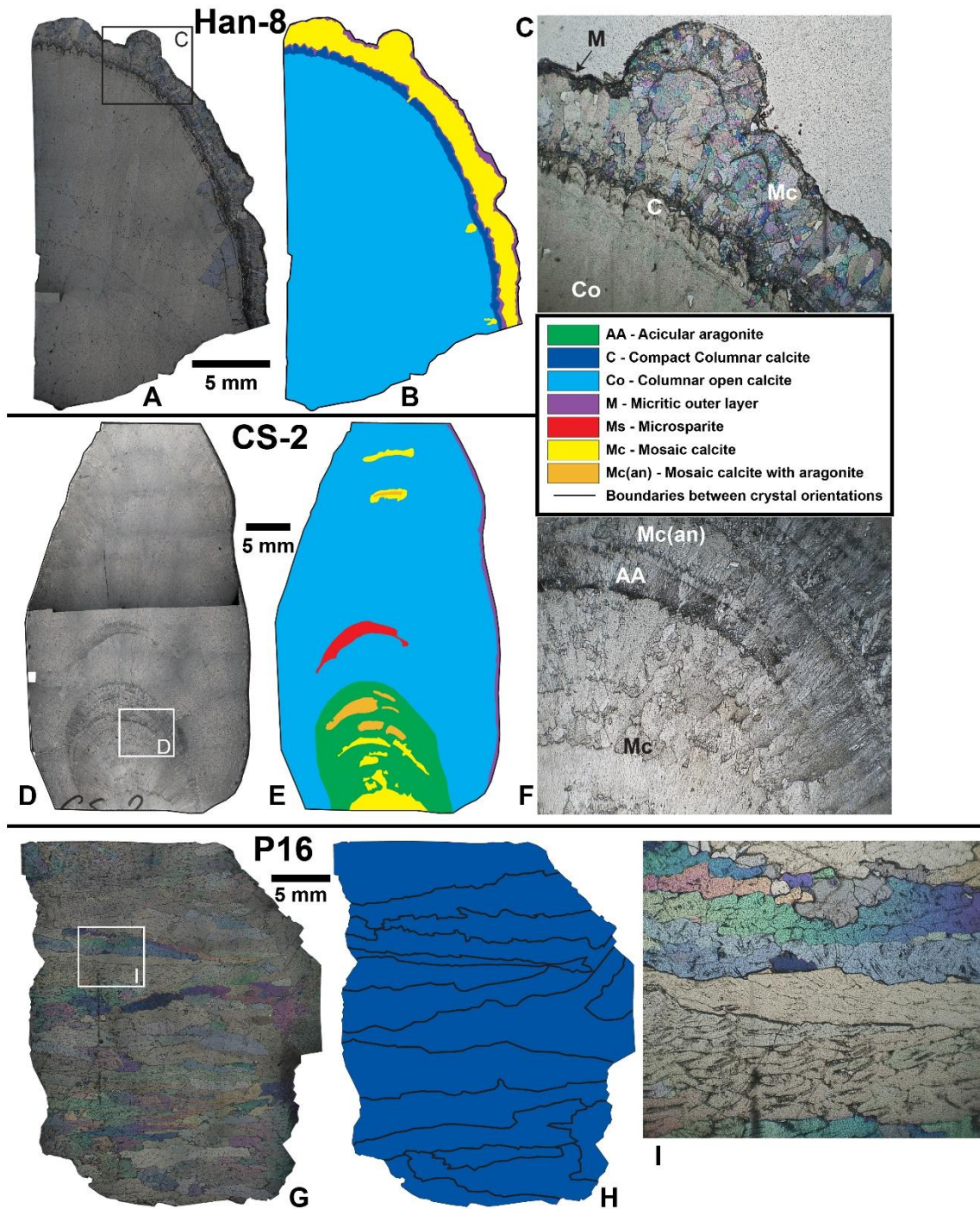


Figure 3: Overview of the results of microscopic investigation of crystal fabrics of thin sections made of samples Han-8, CS-2 and P16. (A) Composite of 25x magnification XPL images of the entire surface of sample Han-8. The insert shows the location of the micrograph depicted in (C). (B) Classification of crystal fabrics in the micrograph composite of sample Han-8. See legend at bottom right of the figure. (C) Detail of the top edge of Han-8 showing the expression of the outer micritic layer (M), mosaic calcite layer (Mc) and compact (C) and open (Co) columnar calcite interior. (D) Composite of 25x magnification PPL microscopic images of sample CS-2. (E) Classification of mineral fabrics in CS-2. (F) Detail of the bottom edge of CS-2 showing mosaic calcite with aragonite (Mc(an)) and acicular aragonite (AA). (G) Composite of 25x magnification XPL images of the entire surface of sample P16. The insert shows the location of the micrograph depicted in (I). (H) Classification of crystal fabrics in the micrograph composite of sample P16. (I) Detail of the bottom edge of P16 showing various crystal fabrics.

(F) Detail of the partly recrystallized inner aragonite on the basal part of CS-2 highlighting the expression of acicular (radial needle-shaped) preserved aragonite textures (AA) and mosaic calcite replacing the aragonite, either with (Mc(an)) or without (Mc) relict aragonite inclusions. (G) Composite of 25x magnification XPL microscopic images of P16 with variations in color showing various crystal orientations. Insert shows the location of (I). (H) Classification of crystal fabrics in P16, showing that this sample consists fully out of compact columnar calcite with dominant shifts in crystal orientations within the sample indicated by black lines. (I) Detailed XPL micrograph of the compact columnar calcite in P16 showing clear transitions between zones of different crystal orientations.

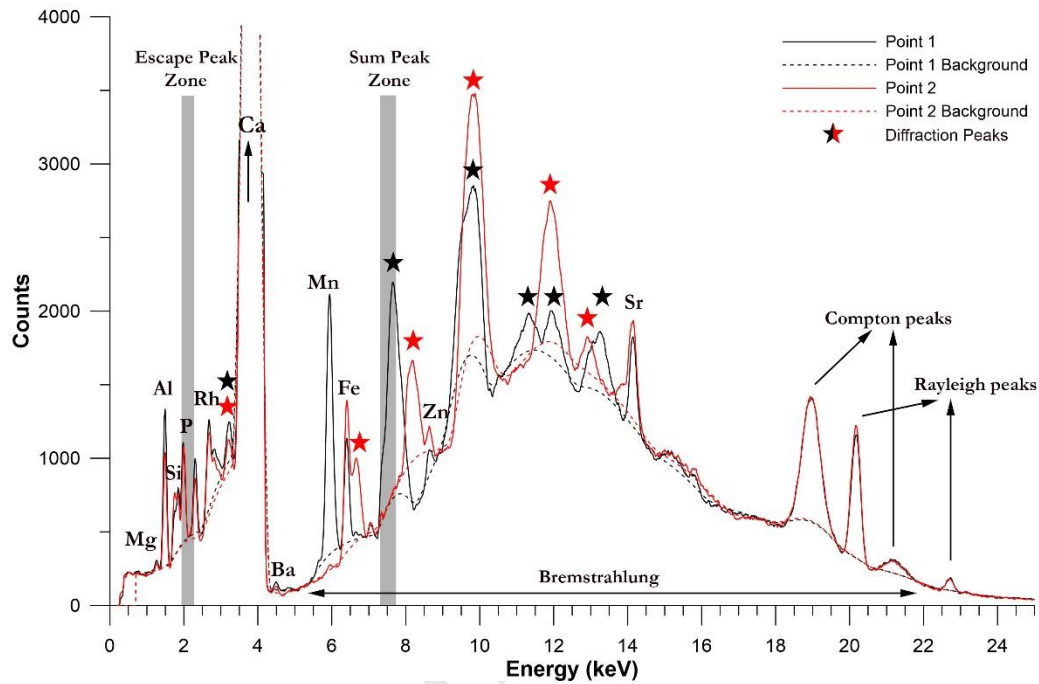


Figure 4: Energy spectra of MEX-1 P1 (black) and P2 (red) (for location, see Fig. 1). Dashed lines mark the background of the spectra. For explanation about Bremstrahlung, Compton peaks and Rayleigh peaks, see text. The part of the energy spectrum where the Sum and Escape peaks of Ca occur are shaded in grey. Stars indicate the diffraction peaks. Notice how the location of the diffraction peaks shifts between P1 and P2. Measurement time: 90 s, energy: 50 keV, 600 μ A.

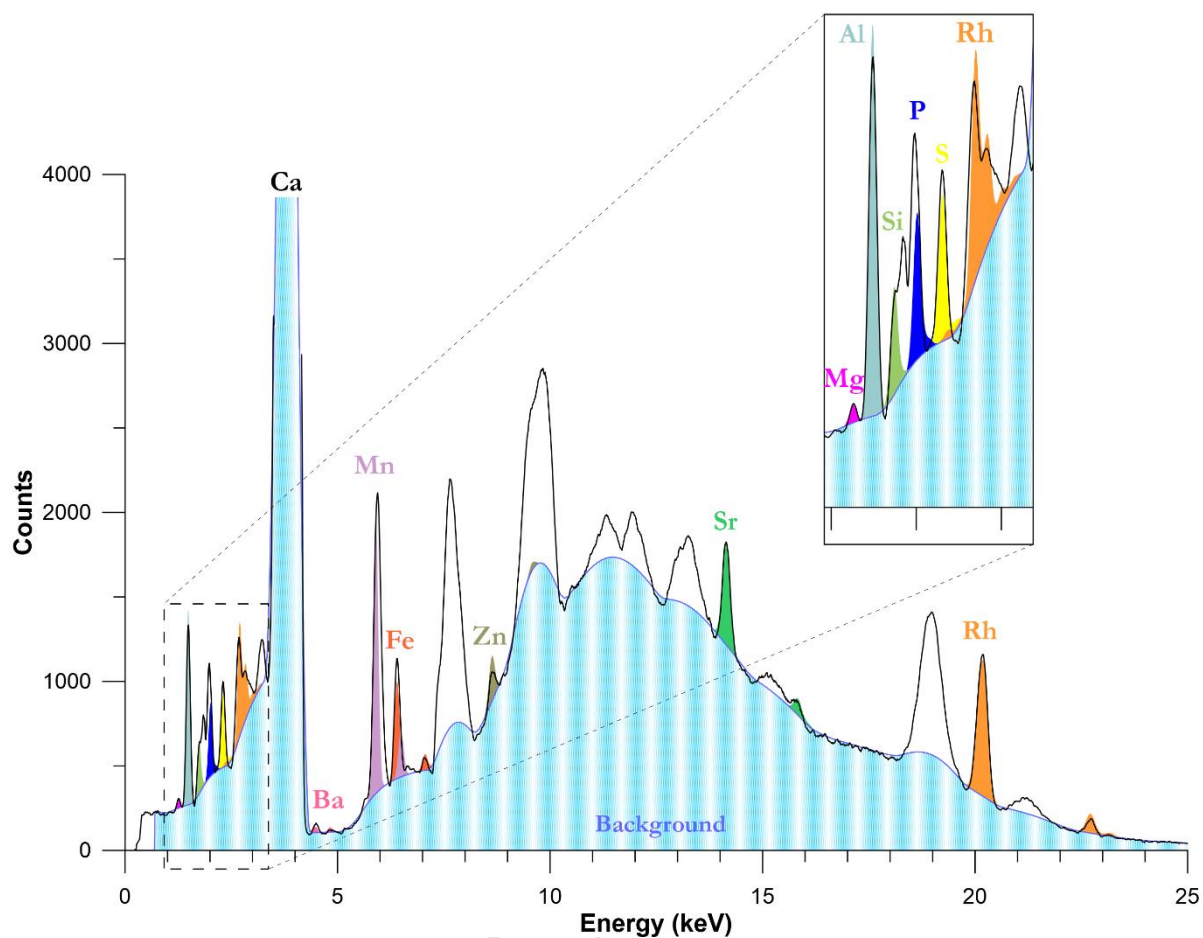


Figure 5: Deconvolution of the energy spectrum of a single-spot measurement on sample MEX-1 (P1). The colored area shows the part of the peaks used for the integration. Striped? Background is indicated in light blue. Notice the occurrence of several large diffraction peaks between 7 and 14 keV (see Fig. 4). Measurement time: 90 s, energy: 50 keV, 600 μ A.

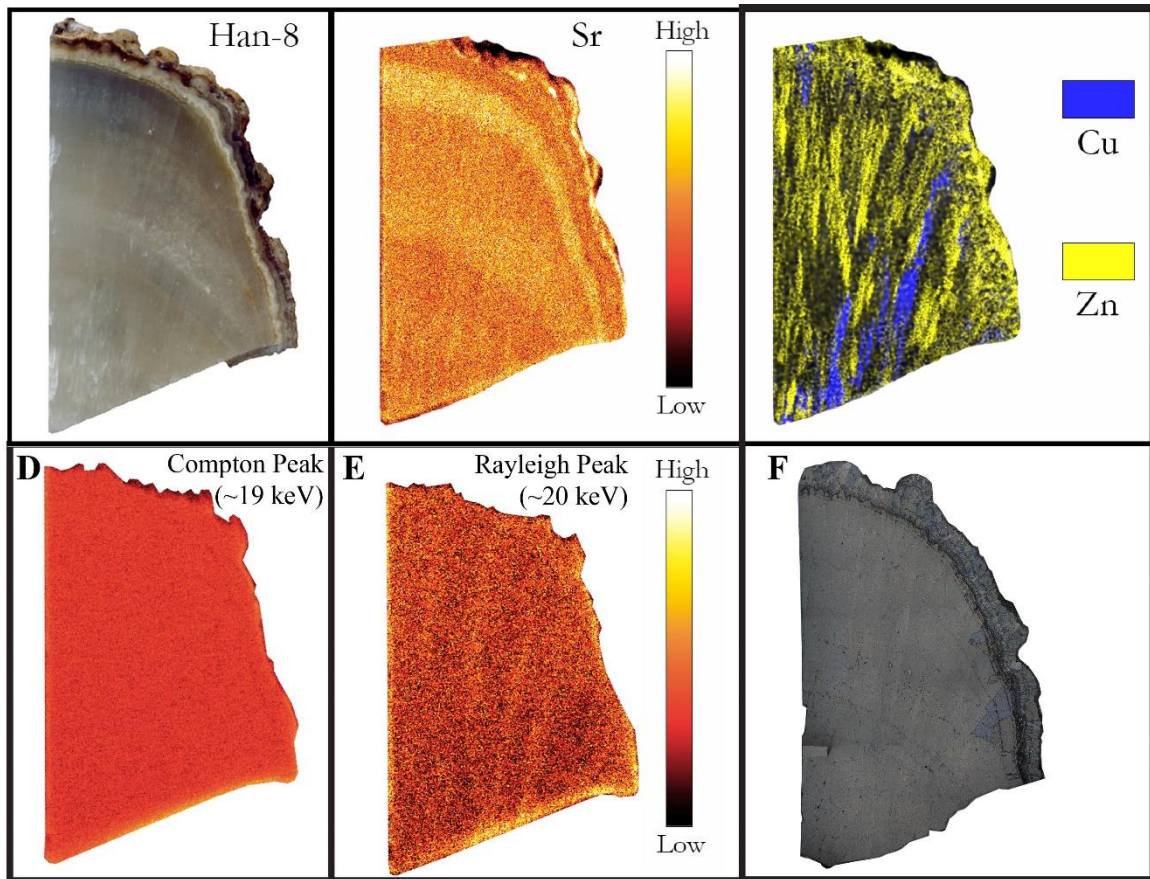


Fig. 6: (A) Top part of Han-8 and corresponding μ XRF maps showing (B) Sr, (C) Cu and Zn, (D) Area under the Compton Peak (~ 19 keV) formed by inelastic scattering of X-rays, (E) Area under the Rayleigh Peak (~ 20 keV) formed by elastic scattering of X-rays (see Fig. 4) and (F) A thin section microscopy composite the sample (see Fig. 3). Distribution of Sr follows the speleothem layering. Zn and Cu do not represent elemental distributions but rather diffraction, which follows the orientation of the calcite crystals. This diffraction is also reflected in the map of the Rayleigh Peak (E), while the Compton Peak (D) does not show this pattern.

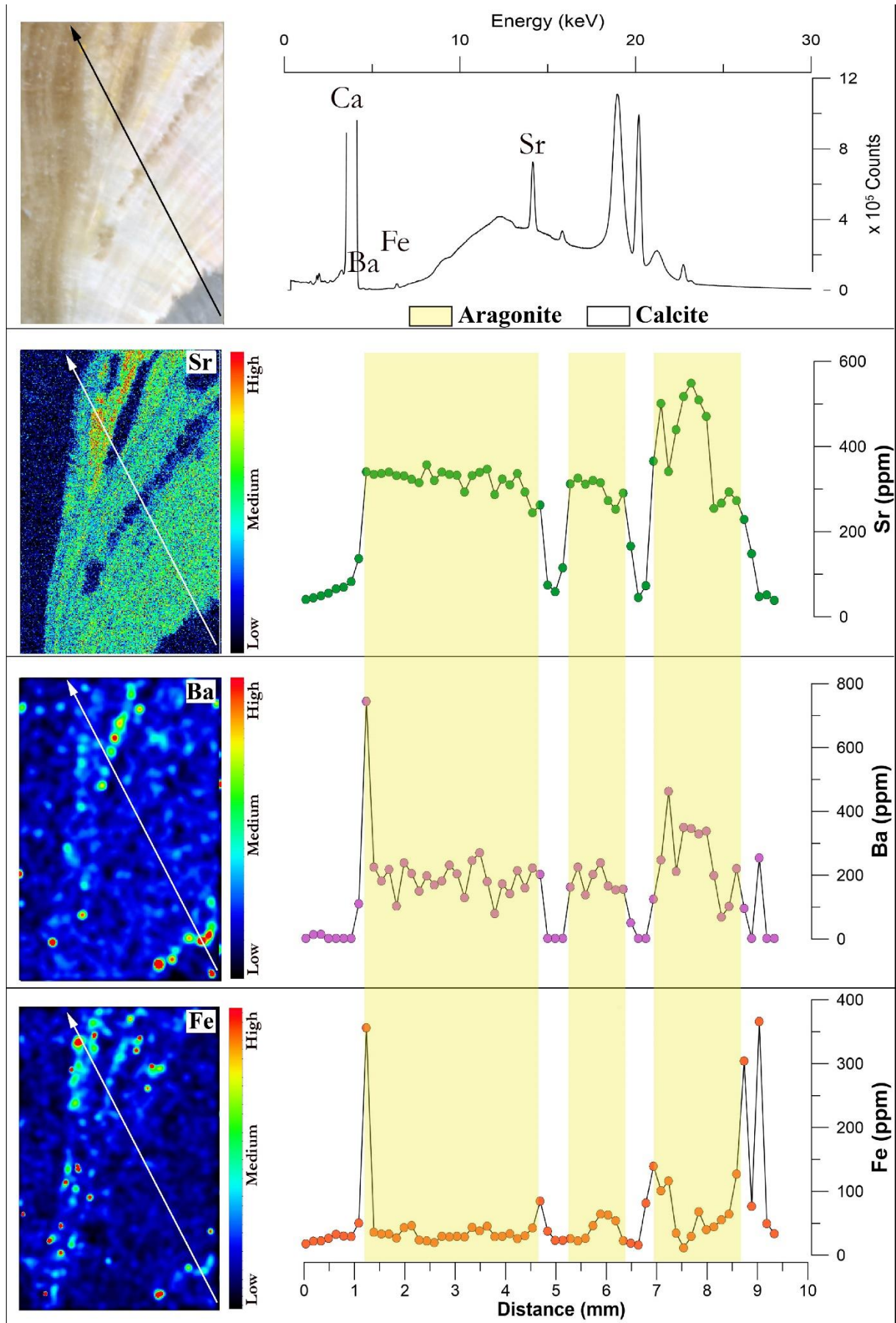


Figure 7: Area maps of sample CS-2 which is mixed calcite aragonite. The milky white parts represent the aragonite. For the location of map on the sample, see red rectangle in Fig. 1. (A) The spectrum of the aragonite part. Notice that nearly no diffraction peaks occur compared to calcite spectra (Fig. 4). Below are the element distribution maps of (B) Sr, (C) Ba and (D) Fe. The line represents a transect of single point measurements (90 s per point) to obtain quantitative data on the elements of interest.

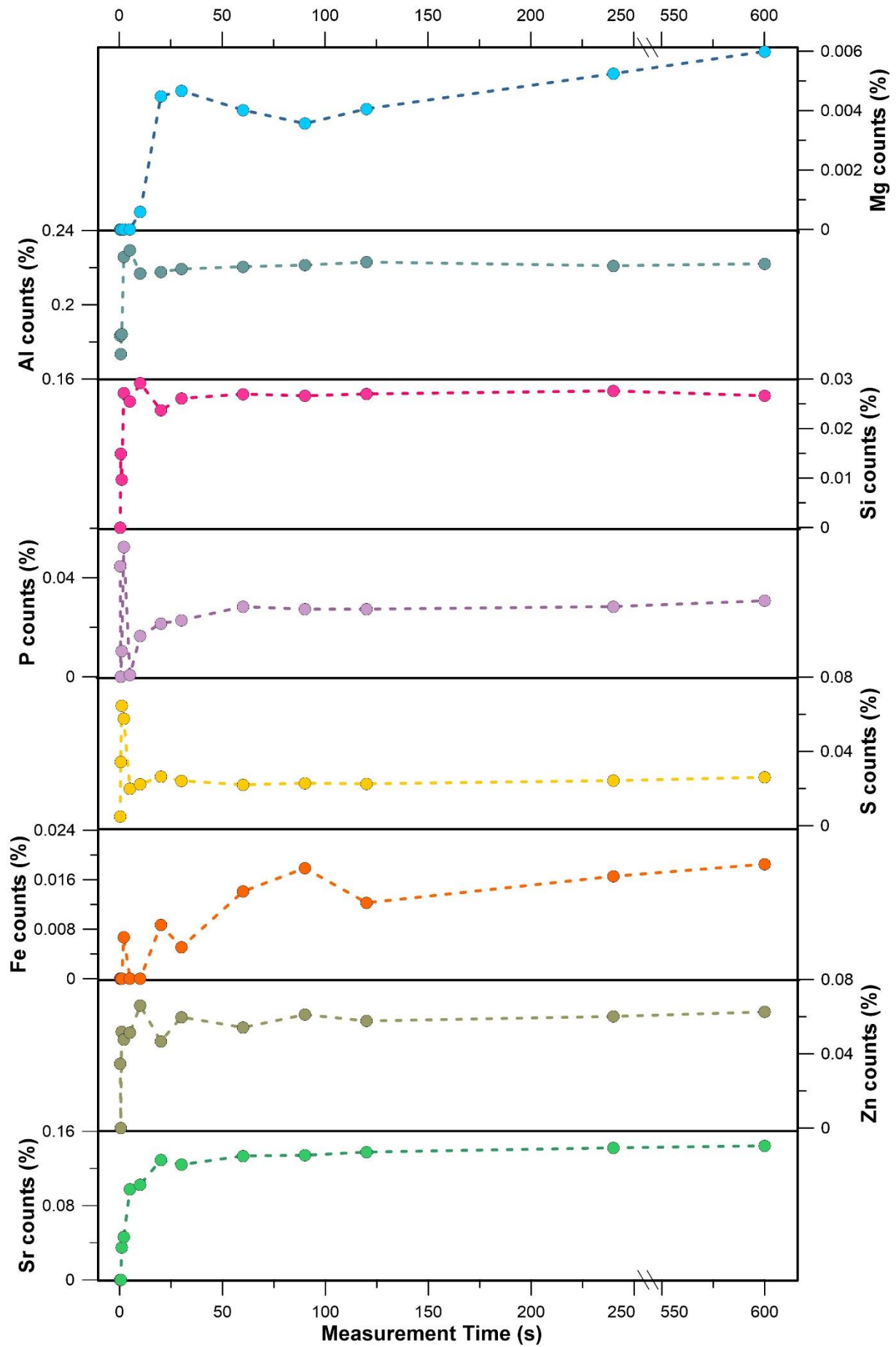


Figure 8: Plot showing the effect of measurement time. Analysis carried out on the sample Han-9 (see red dot in Fig. 1 for the location). Counts of each element are expressed as a percentage of the total amount of counts.

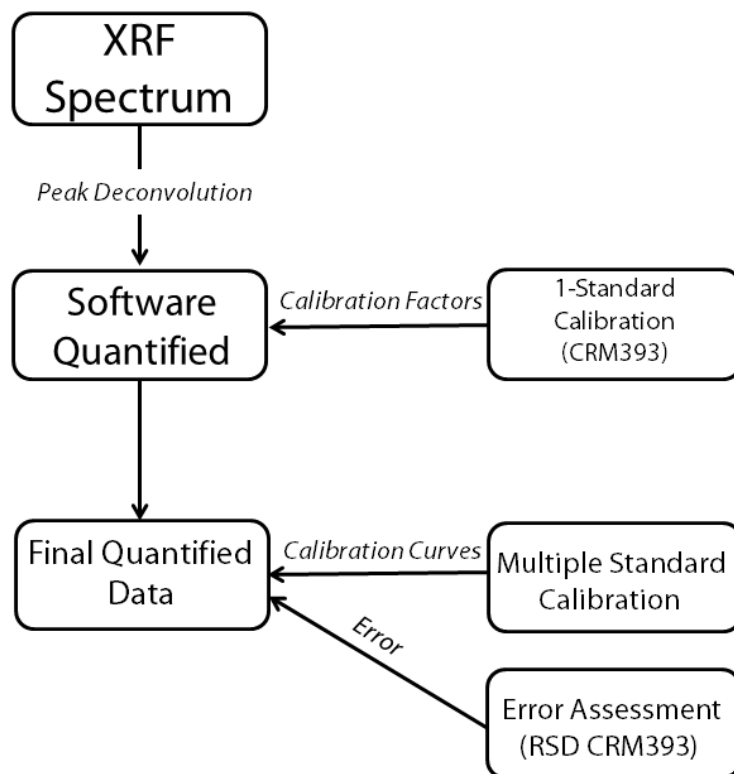


Figure 9: Workflow of the quantification-calibration process presented in this study.

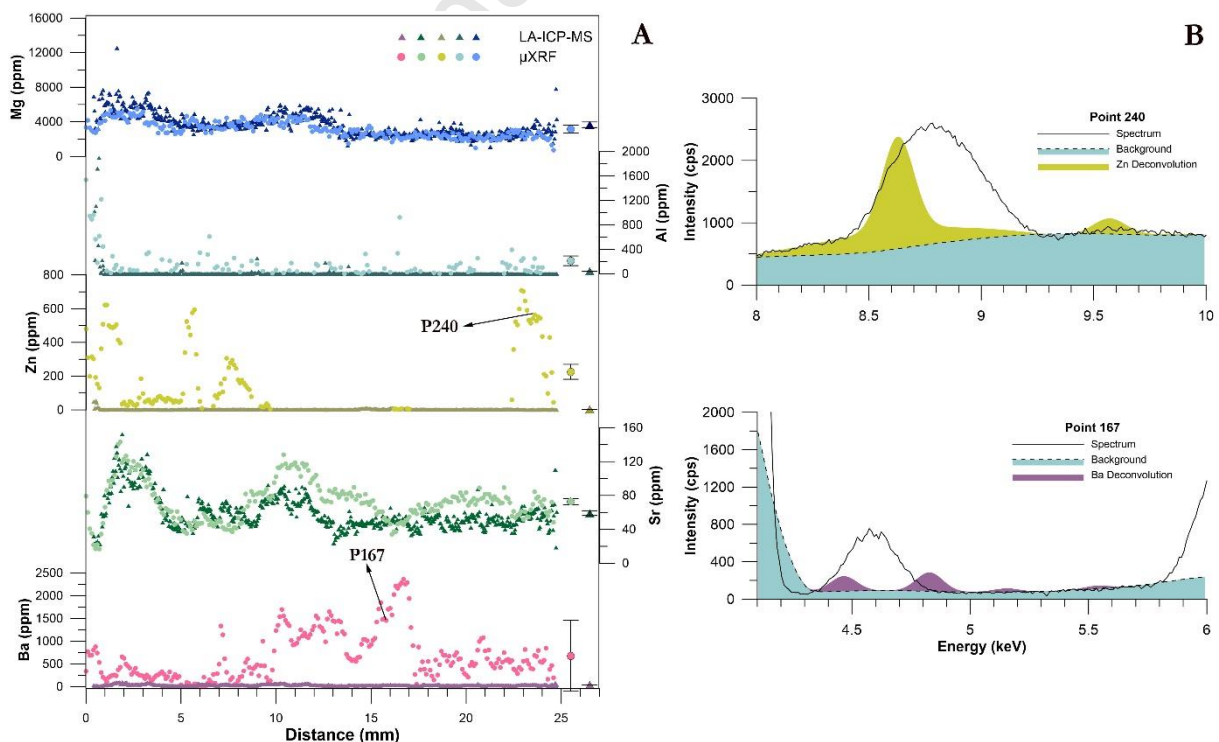


Figure 10: A) comparison of LA-ICP-MS (triangles) and μ XRF (circles) measurements of Mg, Al, Zn, Sr and Ba on sample Han-8. Calculated errors are displayed on the right side of the graph. A good correlation for Mg and Sr can be observed, whereas the correlation of Al, Zn and Ba is very poor. B) spectra of two points (P167 and P240) showing the overlap of diffraction peaks with the Zn and Ba element peaks, resulting in a bad deconvolution and incorrectly quantified μ XRF results.

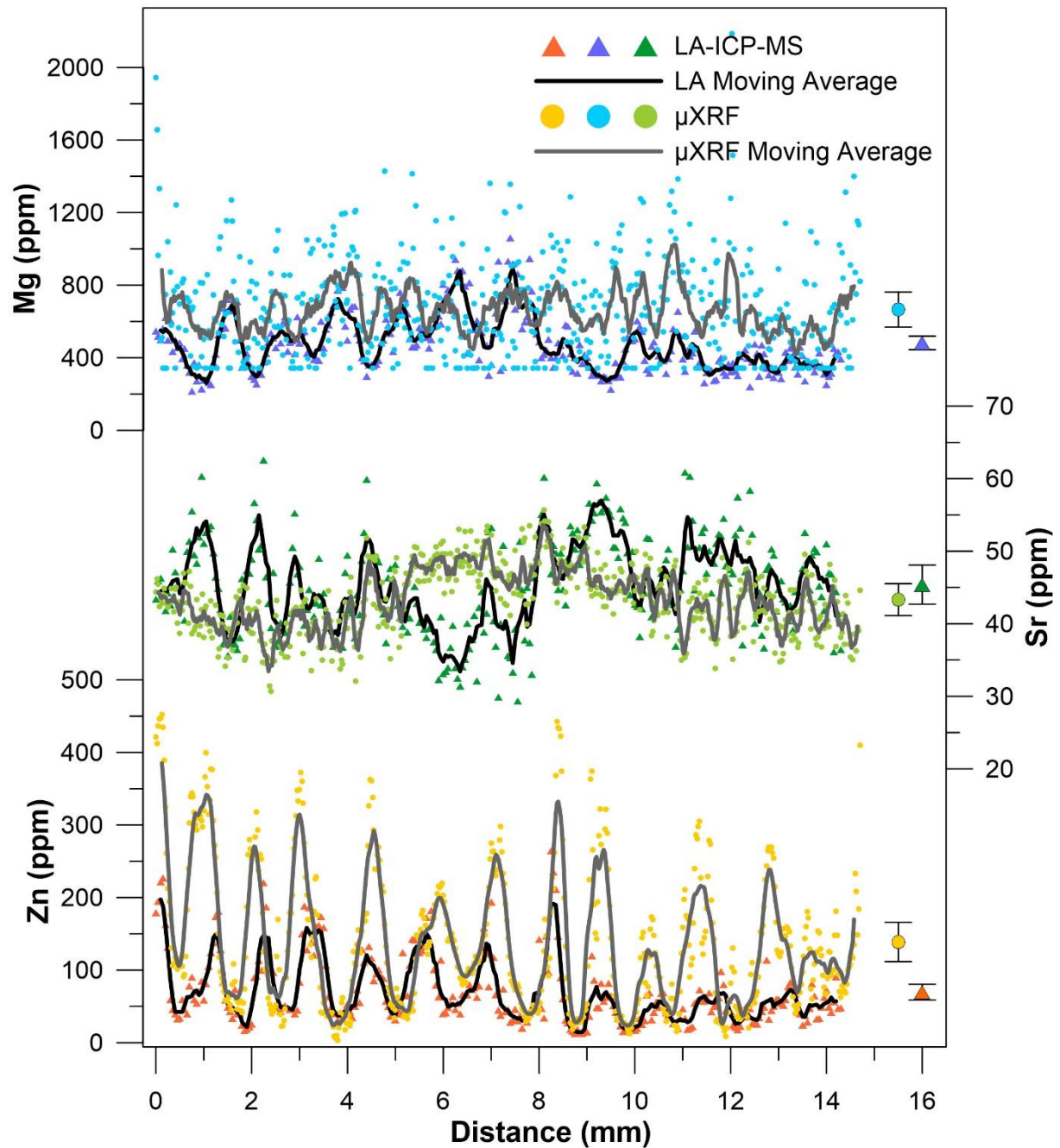


Figure 11: Results for Mg, Sr and Zn of a transect measured by both LA-ICP-MS (triangles) and μ XRF (circles) on the annually laminated speleothem sample P16 (Fig. 1). Errors are shown on the right side of the graphs.

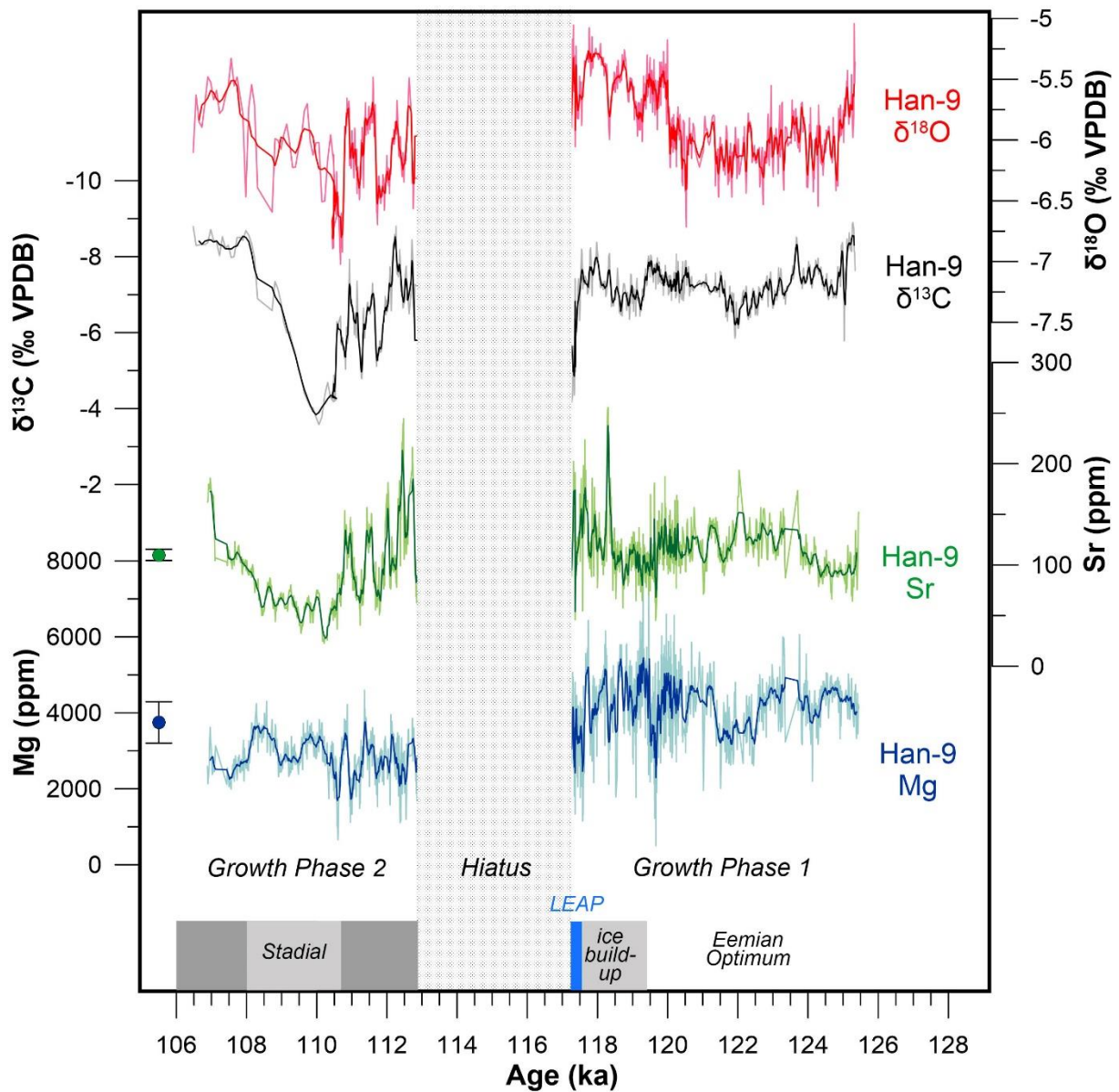


Figure 12: Multiproxy study of Han-9 showing $\delta^{13}\text{C}$, $\delta^{18}\text{O}$, Sr and Mg. Errors of the μXRF data are displayed on the left. This part of the stalagmite is characterized by two growth phases (1 & 2) separated by a hiatus. The interpretation of paleoclimate is given in the figure. For more information about the age-depth model, the stable isotope data or the paleoclimate interpretation, see Vansteenberghe et al. (2016).

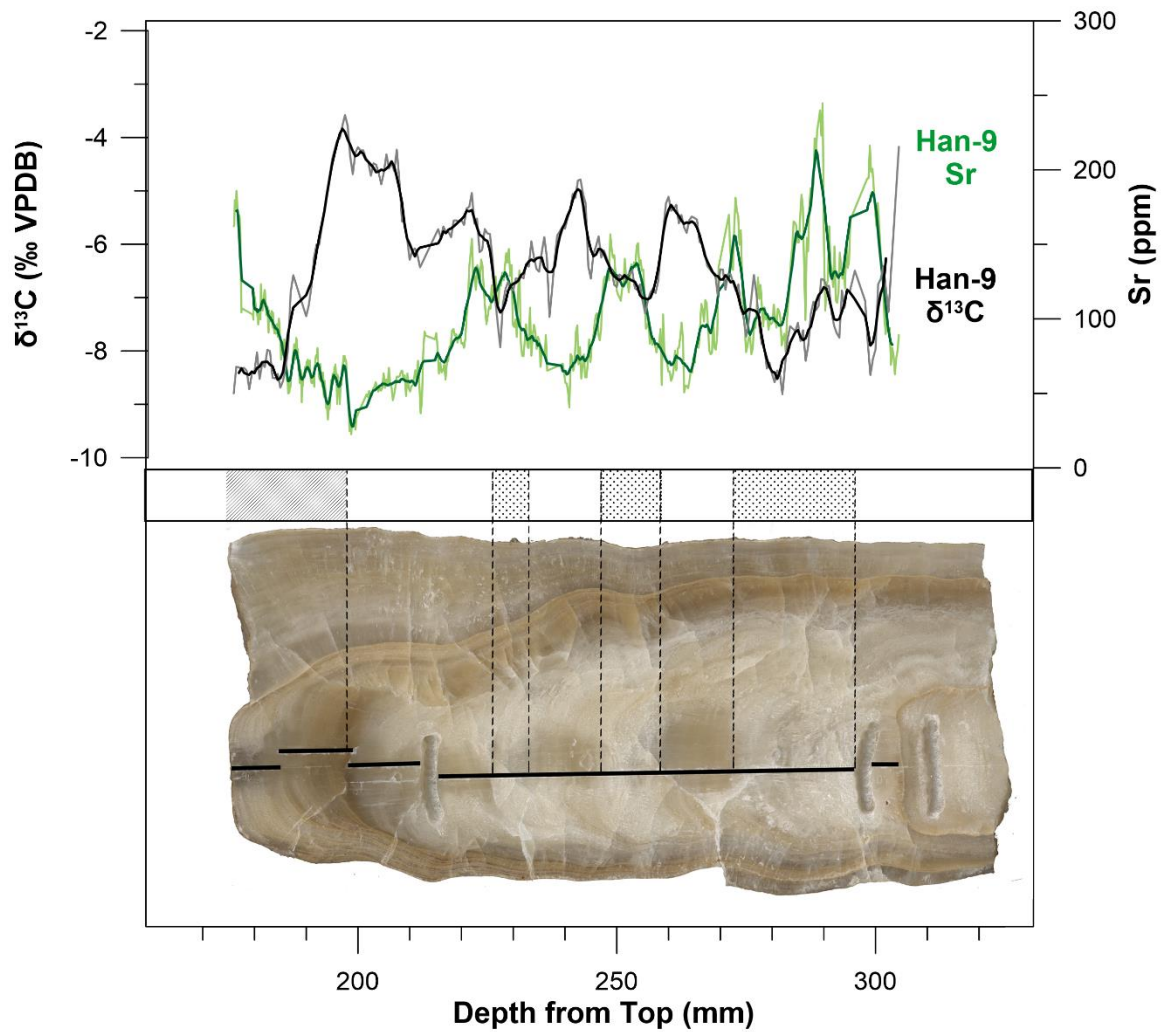


Figure 13: Han-9 (growth phase 2) Sr concentration and $\delta^{13}\text{C}$ variations plotted against distance. $\delta^{13}\text{C}$ axis has a normal orientation. An image of growth phase 2 is displayed below, together with the interpretation of the stalagmite morphology. White boxes represent the dense and darker morphology and filled boxes indicate coarser and whiter morphologies. A clear link between Sr, $\delta^{13}\text{C}$ and speleothem morphology can be observed.

Sample	Cave & Location	Age	Mineralogy	[Mg]	[Sr]	[Ba]	Reference(s)
Han-9	Han-sur-Lesse, Belgium	125.3-97 ka	Calcite stalagmite	3700	110	460	Vansteenberge et al. (2016)
Han-8	Han-sur-Lesse, Belgium	122-111 ka	Calcite stalagmite	4000	75	600	/
CS-2	China	Unknown	Calcite/aragonite stalactite	6700	350	200	/
Mex-1	Cacahualmilpa Cave, Mexico	~50 ka	Calcite stalagmite	1300	170	<LLD	/
P16	Han-sur-Lesse Cave, Belgium	Holocene, ~1600 CE	Calcite stalagmite	600	44	160	Verheyden et al. (2006), Van Rampelbergh et al. (2015), Vansteenberge et al. (in review)

Table 1: information of each sample used in this study. Images of the samples are provided in Fig. 1. Concentrations of Mg, Sr and Ba are rounded averages through the sample and serve to illustrate variability between samples.

	Mg	Al	Si	P	S	Ca	Mn	Fe	Zn	Sr	Ba
Slope	1.15	3.53	1.10	60.14	31.26	1.11	1.23	1.00	1.76	0.97	2.72
Error	0.05	0.83	0.28	86.16	44.18	0.04	0.15	0.52	81.90	0.11	4.51
Intercept	342.93	-969.40	-605.05	-2541.77	-1228.26	-43458.29	-12.75	-4.89	-22.49	13.02	2.06
Error	299.31	448.55	4123.77	3787.70	1870.67	15671.31	16.45	130.48	1947.93	23.19	71.39
Pearson's r	1.00	0.90	0.90	0.98	0.07	1.00	1.00	1.00	0.93	1.00	0.99
LLD ($\mu\text{g/g}$)	491	161	53	65	38	343	7.5	5.1	2.7	8.4	15

Table 2: The results of Deming regression for the construction of calibration lines for a range of trace elements measured with μXRF using carbonate reference materials. The corresponding calibration curves are provided in the supplementary information.

Full Record	Mg	Sr	$\delta^{13}\text{C}$	$\delta^{18}\text{O}$
Mg	1.00	0.16	-0.35	0.35
Sr		1.00	-0.40	0.26
$\delta^{13}\text{C}$			1.00	-0.30
$\delta^{18}\text{O}$				1.00
Growth Phase 1				
Mg	1.00	-0.09	-0.19	0.06
Sr		1.00	0.03	0.02
$\delta^{13}\text{C}$			1.00	0.02
$\delta^{18}\text{O}$				1.00
Growth Phase 2				
Mg	1.00	0.09	0.04	0.32
Sr		1.00	-0.64	0.40
$\delta^{13}\text{C}$			1.00	-0.45
$\delta^{18}\text{O}$				1.00

Table 3: Pearson's coefficient of correlation (r) of the different proxies used in Han-9. r was determined on the full record and on the two growth phases separately. Color intensity reflects the degree of correlation with red for $r < 1$ and blue for $r \geq 1$.

References

- Adcock, R.J.C.F.p.d.M., 1878, A Problem in Least Squares. The Analyst, 5, 53-54.
- Bar-Matthews, M., Ayalon, A., Kaufman, A. and Wasserburg, G.J., 1999, The Eastern Mediterranean paleoclimate as a reflection of regional events: Soreq cave, Israel. Earth and Planetary Science Letters, 166, 85-95.
- Beckhoff, B., Kanngießer, B., Langhoff, N., Wedell, R. and Wolff, H., 2006, Handbook of practical X-Ray Fluorescence analysis. Springer.
- Belli, R., Borsato, A., Frisia, S., Drysdale, R., Maas, R., Greig, A., 2017. Investigating the hydrological significance of stalagmite geochemistry (Mg, Sr) using Sr isotope and particulate element records across the Late Glacial-to-Holocene transition. Geochimica et Cosmochimica Acta 199, 247–263. <https://doi.org/10.1016/j.gca.2016.10.024>
- Boch, R., Cheng, H., Spötl, C., Edwards, R.L., Wang, X., Häuselmann, P., 2011. NALPS: a precisely dated European climate record 120–60 ka. Climate of the Past 7, 1247–1259. <https://doi.org/10.5194/cp-7-1247-2011>
- Borsato, A., Frisia, S., Fairchild, I.J., Somogyi, A. and Susini, J., 2007, Trace element distribution in annual stalagmite laminae mapped by micrometer-resolution X-ray fluorescence: Implications for incorporation of environmentally significant species. Geochimica Et Cosmochimica Acta, 71, 1494-1512.
- Buckles, J. and Rowe, H.D., 2016, Development and optimization of microbeam X-ray fluorescence analysis of Sr in speleothems. Chemical Geology, 426, 28-32.
- Cui, Y.F., Wang, Y.J., Cheng, H., Zhao, K. and Kong, X.G., 2012, Isotopic and lithologic variations of one precisely-dated stalagmite across the Medieval/LIA period from Heilong Cave, central China. Clim. Past, 8, 1541-1550.

- Dandurand, G., Maire, R., Ortega, R., Devès, G., Lans, B., Morel, L., Perroux, A.-S., Vanara, N., Bruxelles, L., Jaillet, S., Billy, I., Martinez, P., Ghaleb, B. and Valla, F., 2011, X-ray fluorescence microchemical analysis and autoradiography applied to cave deposits: speleothems, detrital rhythmites, ice and prehistoric paintings. *Géomorphologie : Relief, Processus, Environnement*, 17, 20.
- Day, C.C., Henderson, G.M., 2013. Controls on trace-element partitioning in cave-analogue calcite. *Geochimica et Cosmochimica Acta* 120, 612–627. <https://doi.org/10.1016/j.gca.2013.05.044>
- de Winter, N.J. and Claeys, P. (2017) Micro X-ray fluorescence (μ XRF) line scanning on Cretaceous rudist bivalves: A new method for reproducible trace element profiles in bivalve calcite. *Sedimentology*, 64, 231-251.
- de Winter, N.J., Goderis, S., Dehairs, F., Jagt, J.W.M., Fraaije, R.H.B., Van Malderen, S.J.M., Vanhaecke, F. and Claeys, P., 2017a Tropical seasonality in the late Campanian (late Cretaceous): Comparison between multiproxy records from three bivalve taxa from Oman. *Palaeogeography, Palaeoclimatology, Palaeoecology*.
- de Winter, N.J., Sinnesael, M., Makarona, C., Vansteenberge, S., Claeys, P., 2017b. Trace element analyses of carbonates using portable and micro-X-ray fluorescence: performance and optimization of measurement parameters and strategies. *Journal of Analytical Atomic Spectrometry* 32, 1211–1223.
- Deming, W.E., 1943, Statistical adjustment of data. John Wiley & Sons.
- Fairchild, I.J., Borsato, A., Tooth, A.F., Frisia, S., Hawkesworth, C.J., Huang, Y.M., McDermott, F. and Spiro, B., 2000, Controls on trace element (Sr-Mg) compositions of carbonate cave waters: implications for speleothem climatic records. *Chemical Geology*, 166, 255-269.
- Fairchild, I.J., Smith, C.L., Baker, A., Fuller, L., Spotl, C., Matthey, D., McDermott, F. and Eimp, 2006, Modification and preservation of environmental signals in speleothems. *Earth-Science Reviews*, 75, 105-153.
- Fairchild, I.J. and Treble, P.C., 2009, Trace elements in speleothems as recorders of environmental change. *Quaternary Science Reviews*, 28, 449-468.
- Finné, M., Kylander, M., Boyd, M., Sundqvist, H.S. and Löwemark, L., 2015, Can XRF scanning of speleothems be used as a non-destructive method to identify paleoflood events in caves? *International Journal of Speleology*, 17-23.
- Frisia, S., Borsato, A., Fairchild, I.J., McDermott, F., 2000. Calcite fabrics, growth mechanisms, and environments of formation in speleothems from the Italian Alps and southwestern Ireland. *Journal of Sedimentary Research* 70, 1183–1196.
- Frisia, S., Borsato, A., Fairchild, I.J., McDermott, F., Selmo, E.M., 2002. Aragonite-Calcite Relationships in Speleothems (Grotte De Clamouse, France): Environment, Fabrics, and Carbonate Geochemistry. *Journal of Sedimentary Research* 72, 687–699. <https://doi.org/10.1306/020702720687>
- Frisia, S., Borsato, A., Susini, J. and Somogyi, A., 2005. Climate forcings and their influence on Alpine history as reconstructed through the application of synchrotron-based X-ray microfluorescence on layered stalagmites. *Archaeometry*, 47, 209-219.
- Frisia, S., Borsato, A., Drysdale, R.N., Paul, B., Greig, A. and Cotte, M., 2012. A re-evaluation of the palaeoclimatic significance of phosphorus variability in speleothems revealed by high-resolution synchrotron micro XRF mapping. *Climate of the Past*, 8, 2039-2051.

- Frisia, S., 2015. Microstratigraphic logging of calcite fabrics in speleothems as tool for palaeoclimate studies. *International Journal of Speleology* 44.
<https://doi.org/10.5038/1827-806X.44.1.1>
- Gaughlitz, G. and Moore, D.S., 2014. *Handbook of Spectroscopy*. Wiley, 1993 pp.
- Hartland, A., Fairchild, I.J., Lead, J.R., Borsato, A., Baker, A., Frisia, S. and Baalousha, M., 2012. From soil to cave: Transport of trace metals by natural organic matter in karst dripwaters. *Chemical Geology*, 304, 68-82.
- Huang, H.M., Fairchild, I.J., Borsato, A., Frisia, S., Cassidy, N.J., McDermott, F. and Hawkesworth, C.J., 2001. Seasonal variations in Sr, Mg and P in modern speleothems (Grotta di Ernesto, Italy). *Chemical Geology*, 175, 429-448.
- Jamieson, R.A., Baldini, J.U.L., Brett, M.J., Taylor, J., Ridley, H.E., Ottley, C.J., Prufer, K.M., Wassenburg, J.A., Scholz, D. and Breitenbach, S.F.M., 2016. Intra- and inter-annual uranium concentration variability in a Belizean stalagmite controlled by prior aragonite precipitation: A new tool for reconstructing hydro-climate using aragonitic speleothems. *Geochimica Et Cosmochimica Acta*, 190, 332-346.
- Jenkins, R., 1999. *X-Ray Fluorescence Spectrometry*, 2nd Edition. Wiley, 232 pp.
- Johnson, K.R., Hu, C.Y., Belshaw, N.S. and Henderson, G.M., 2006. Seasonal trace-element and stable-isotope variations in a Chinese speleothem: The potential for high-resolution paleomonsoon reconstruction. *Earth and Planetary Science Letters*, 244, 394-407.
- Kummell, C.H., 1879. Reduction of Observation Equations Which Contain More Than One Observed Quantity. *The Analyst*, 6, 97-105.
- Kurunczi, S., Torok, S. and Chevallier, P., 2001. A micro-XRF study of the element distribution on the growth front of mussel shell (Species of *Unio crassus* Retzius). *Mikrochimica Acta*, 137, 41-48.
- Lachniet, M.S., 2009. Climatic and environmental controls on speleothem oxygen-isotope values. *Quaternary Science Reviews*, 28, 412-432.
- Lazareth, C.E., Putten, E.V., André, L. and Dehairs, F., 2003. High-resolution trace element profiles in shells of the mangrove bivalve *Isognomon ehippium*: a record of environmental spatio-temporal variations? *Estuarine, Coastal and Shelf Science*, 57, 1103-1114.
- Mattey, D.P., Fairchild, I.J., Atkinson, T.C., Latin, J.-P., Ainsworth, M., Durell, R., 2010. Seasonal microclimate control of calcite fabrics, stable isotopes and trace elements in modern speleothem from St Michaels Cave, Gibraltar. *Geological Society, London, Special Publications* 336, 323-344.
- McDermott, F., 2004. Palaeo-climate reconstruction from stable isotope variations in speleothems: a review. *Quaternary Science Reviews*, 23, 901-918.
- Pearce, N.J.G., Perkins, W.T., Westgate, J.A., Gorton, M.P., Jackson, S.E., Neal, C.R. and Chenery, S.P., 1997. A Compilation of New and Published Major and Trace Element Data for NIST SRM 610 and NIST SRM 612 Glass Reference Materials. *Geostandards Newsletter*, 21, 115-144.
- Potts, P.J. and Webb, P.C., 1992. X-RAY-FLUORESCENCE SPECTROMETRY. *Journal of Geochemical Exploration*, 44, 251-296.
- R Core Team, 2013. *R: a language and environment for statistical computing*. R Foundation for Statistical Computing, Vienna, Austria.
- Rasmussen, S.O., Bigler, M., Blockley, S.P., Blunier, T., Buchardt, S.L., Clausen, H.B., Cvijanovic, I., Dahl-Jensen, D., Johnsen, S.J., Fischer, H., Gkinis, V., Guillevic, M., Hoek, W.Z., Lowe, J.J., Pedro, J.B., Popp, T., Seierstad, I.K., Steffensen, J.P., Svensson, A.M., Vallelonga, P., Vinther, B.M., Walker, M.J.C., Wheatley, J.J. and Winstrup, M., 2014. A stratigraphic framework for abrupt climatic

- changes during the Last Glacial period based on three synchronized Greenland ice-core records: refining and extending the INTIMATE event stratigraphy. *Quaternary Science Reviews*, 106, 14-28.
- Regattieri, E., Zanchetta, G., Drysdale, R.N., Isola, I., Woodhead, J.D., Hellstrom, J.C., Giaccio, B., Greig, A., Banerjee, I., Dotsika, E., 2016. Environmental variability between the penultimate deglaciation and the mid Eemian: Insights from Tana che Urla (central Italy) speleothem trace element record. *Quaternary Science Reviews* 152, 80–92.
<https://doi.org/10.1016/j.quascirev.2016.09.027>
- Richter, T.O., van der Gaast, S., Koster, B., Vaars, A., Giesels, R., de Stigter, H.C., De Haas, H. and van Weering, T.C.E., 2006. The Avaatech XRF Core Scanner: technical description and applications to NE Atlantic sediments. Geological Society, London, Special Publications, 267, 39.
- Rousseau, R., 2013. How to Apply the Fundamental Parameters Method to the Quantitative X-ray Fluorescence Analysis of Geological Materials. *Journal of Geosciences and Geomatics*, 1, 1-7.
- Rousseau, R.M., 1984a. FUNDAMENTAL ALGORITHM BETWEEN CONCENTRATION AND INTENSITY IN XRF ANALYSIS .1. THEORY. *X-Ray Spectrometry*, 13, 115-120.
- Rousseau, R.M., 1984b. FUNDAMENTAL ALGORITHM BETWEEN CONCENTRATION AND INTENSITY IN XRF ANALYSIS .2. PRACTICAL APPLICATION. *X-Ray Spectrometry*, 13, 121-125.
- Rousseau, R.M. and Boivin, J.A., 1998. The Fundamental Algorithm: a natural extension of the Sherman Equation Part I: Theory. *The Rigaku Journal*, 15, 16.
- Rousseau, R.M. and Bouchard, M., 1986. FUNDAMENTAL ALGORITHM BETWEEN CONCENTRATION AND INTENSITY IN XRF ANALYSIS .3. EXPERIMENTAL-VERIFICATION. *X-Ray Spectrometry*, 15, 207-215.
- Shackley, M.S., 2011. X-Ray Fluorescence spectrometry (XRF) in Geoarchaeology. Springer, 202 pp.
- Sherman, J., 1955. The theoretical derivation of fluorescent X-ray intensities from mixtures. *Spectrochimica Acta*, 7, 283-306.
- Sutton, S.R., Rivers, M.L., Smith, J.V., 1986. Synchrotron X-ray fluorescence: diffraction interference. *Analytical Chemistry* 58, 2167–2171.
- Van Rangelbergh, M., Verheyden, S., Allan, M., Quinif, Y., Cheng, H., Edwards, L.R., Keppens, E. and Claeys, P., 2015. A 500-year seasonally resolved delta O-18 and delta C-13, layer thickness and calcite aspect record from a speleothem deposited in the Han-sur-Lesse cave, Belgium. *Climate of the Past*, 11, 789-802.
- Vanghi, V., Borsato, A., Frisia, S., Howard, D.L., Gloy, G., Hellstrom, J., Bajo, P., 2019. High-resolution synchrotron X-ray fluorescence investigation of calcite coralloid speleothems: Elemental incorporation and their potential as environmental archives. *Sedimentology* 0.
<https://doi.org/10.1111/sed.12607>
- Vansteenberghe, S., Verheyden, S., Cheng, H., Edwards, R.L., Keppens, E. and Claeys, P., 2016. Paleoclimate in continental northwestern Europe during the Eemian and early Weichselian (125–97 ka): insights from a Belgian speleothem. *Clim. Past*, 12, 1445-1458.
- Vansteenberghe, S., Verheyden, S., Genty, D., Blamart, D., Goderis, S., Van Malderen, S.J.M., Vanhaecke, F., Hodel, F., Gillikin, D., Ek, C., Quinif, Y., Cheng, H., Edwards, R.L., Claeys, P., 2019. Characterizing the Eemian-Weichselian transition in northwestern Europe with three multiproxy speleothem archives from the Belgian Han-sur-Lesse and Remouchamps cave systems. *Quaternary Science Reviews* 208, 21–37. <https://doi.org/10.1016/j.quascirev.2019.01.011>
- Vansteenberghe, S., Winter, N. de, Sinnesael, M., Verheyden, S., Goderis, S., Malderen, S.J.M.V., Vanhaecke, F., Claeys, P., 2019. Reconstructing seasonality through stable isotope and trace element analysis of the Proserpine stalagmite, Han-sur-Lesse Cave, Belgium: indications for

- climate-driven changes during the last 400 years. *Climate of the Past Discussions* 1–32.
<https://doi.org/10.5194/cp-2019-78>
- Verheyden, S., Keppens, E., Fairchild, I.J., McDermott, F. and Weis, D., 2000. Mg, Sr and Sr isotope geochemistry of a Belgian Holocene speleothem: implications for paleoclimate reconstructions. *Chemical Geology*, 169, 131-144.
- Verheyden, S., Baele, J.M., Keppens, E., Genty, D., Cattani, O., Hai, C., Edwards, L., Hucai, Z., Van Strijdonck, M. and Quinif, Y., 2006. The proserpine stalagmite (Han-sur-Lesse cave, Belgium): Preliminary environmental interpretation of the last 1000 years as recorded in a layered speleothem. *Geologica Belgica*, 9, 245-256.
- Verheyden, S., Nader, F.H., Cheng, H.J., Edwards, L.R., Swennen, R., 2008a. Paleoclimate reconstruction in the Levant region from the geochemistry of a Holocene stalagmite from the Jeita cave, Lebanon. *Quaternary Research* 70, 368–381.
- Verheyden S., Genty D., Deflandre G., Quinif Y. and Keppens E., 2008b. Monitoring climatological, hydrological and geochemical parameters in the Père Noël cave (Belgium): Implication for the interpretation of speleothem isotopic and geochemical time-series. *International Journal of Speleology*, 37(3): 221–234.
- Wang, Y.-J., Cheng, H., Edwards, R.L., An, Z.S., Wu, J.Y., Shen, C.-C., Dorale, J.A., 2001. A high-resolution absolute-dated late Pleistocene monsoon record from Hulu Cave, China. *science* 294, 2345–2348.
- Wassenburg, J.A., Immenhauser, A., Richter, D.K., Jochum, K.P., Fietzke, J., Deininger, M., Goos, M., Scholz, D. and Sabaoui, A., 2012. Climate and cave control on Pleistocene/Holocene calcite-to-aragonite transitions in speleothems from Morocco: Elemental and isotopic evidence. *Geochimica et Cosmochimica Acta*, 92, 23-47.
- Weltje, G.J. and Tjallingii, R., 2008. Calibration of XRF core scanners for quantitative geochemical logging of sediment cores: Theory and application. *Earth and Planetary Science Letters*, 274, 423-438.
- Wenk, H.-R., Barber, D.J., Reeder, R.J., 1983. Microstructures in carbonates. *Reviews in Mineralogy and Geochemistry* 11, 301–367.
- Wong, C.I. and Breecker, D.O., 2015. Advancements in the use of speleothems as climate archives. *Quaternary Science Reviews*, 127, 1-18.
- Wu, J.Y., Wang, Y.J., Cheng, H., Kong, X.G. and Liu, D.B., 2012. Stable isotope and trace element investigation of two contemporaneous annually-laminated stalagmites from northeastern China surrounding the "8.2 ka event". *Clim. Past*, 8, 1497-1507.
- Wynn, P.M., Fairchild, I.J., Spotl, C., Hartland, A., Matthey, D., Fayard, B. and Cotte, M., 2014. Synchrotron X-ray distinction of seasonal hydrological and temperature patterns in speleothem carbonate. *Environmental Chemistry*, 11, 28-36.

Declaration of interests

☒ The authors declare that they have no known competing financial interests or personal relationships that could have appeared to influence the work reported in this paper.

☐ The authors declare the following financial interests/personal relationships which may be considered as potential competing interests:

HIGHLIGHTS

- Exploring the use of benchtop μ XRF for speleothem trace element analysis
- Diffraction peaks in the μ XRF spectrum should be treated with care
- Quantification of μ XRF spectra with a multiple-standard calibration is presented
- Validation with LA-ICP-MS confirms the potential of μ XRF in speleothem studies